Geoscience Frontiers 9 (2018) 415–430

HOSTED BY

Contents lists available at ScienceDirect

China University of Geosciences (Beijing)

Geoscience Frontiers

journal homepage: www.elsevier.com/locate/gsf

Research Paper

# Source to sink zircon grain shape: Constraints on selective preservation and significance for Western Australian Proterozoic basin provenance

V. Markwitz [a,*], C.L. Kirkland [b]

[a] School of Earth & Environment, The University of Western Australia, Crawley, WA 6009, Australia
[b] Department of Applied Geology, Centre for Exploration Targeting – Curtin Node, John de Laeter Centre, Institute of Geoscience Research (TIGeR), Curtin University, WA 6045, Australia

ARTICLE INFO

*Article history:*
Received 17 November 2016
Received in revised form
21 March 2017
Accepted 2 April 2017
Available online 29 April 2017
Handling Editor: M. Santosh

*Keywords:*
Zircon grain shape
U–Pb geochronology
Detrital
Whole rock geochemistry
Precambrian

ABSTRACT

The effect of selective preservation during transportation of zircon grains on the detrital age spectrum is difficult to quantify and could potentially lead to systematic bias in provenance analysis. Here we investigate whether the shape of detrital zircon grains holds provenance information and if the grain shape can assist in understanding preservation. We applied multiple linear regression analysis to identify significant shape properties in detrital zircons from Proterozoic metasediments of the Capricorn and Amadeus basins and their Archean and Proterozoic sources in the Yilgarn Craton and the Musgrave Province in Western Australia. Digital images and isotopic data from 819 SIMS U–Pb dated zircons were examined for correlation between grain shape, age, U and Th content. Out of twelve shape descriptors measured, *Minor Axis*, the width of zircon grains perpendicular to the crystallographic c-axis, consistently shows the most significant correlation with isotopic age. In the studied population Archean grains are narrower than Proterozoic grains: the probability that grains wider than 75 μm are Archean is less than 30%.

Calculations of the proportions of source material in sedimentary rocks relative to the proportions of source material in the overall catchment area (erosion parameter '*K*' calculated based on age spectra) produced values typical for mature river systems, with $K = 6$ for the Yilgarn-Capricorn and $K = 5.5$ for the Musgrave-Amadeus source-sink system. For the Yilgarn-Capricorn system, we also calculated '*K*' based on *Minor Axis*, to determine whether grain width can be linked to age populations. Results of the shape-based *K* of 5.3 suggest a similarity between age-based and shape-based '*K*' values, demonstrating that zircon grain width may be a useful discriminator of provenance. Contrary to commonly applied qualitative shape classifications, we found no consistent correlations between shape descriptors of magmatic zircons and the composition of their host rock. While metamict zircons were preferentially removed during transport, the similarities in grain shape and age distribution of magmatic and detrital populations suggest that hydraulic sorting did not have a significant effect. We conclude that transport of zircon grains from magmatic source to sedimentary sink affects their width less than their length.



## 1. Introduction

Detrital zircon geochronology has emerged as a powerful tool to define maximum depositional ages of clastic sediments, reconstruct the provenance of sedimentary rocks, fingerprint and correlate sedimentary units and characterize the magmatic history for large volumes of continental crust (e.g. DeCelles et al., 2007; Kirkland et al., 2007; Gehrels, 2012; Hart et al., 2016; Spencer et al., 2016). Zircon crystals resist a wide range of physical and chemical alteration processes in sedimentary systems and are able to survive multiple erosion and re-deposition cycles (Fedo et al., 2003). An important question related to the use of detrital zircon grains in reconstructing provenance signatures is to what extent the detrital population retains the age or chemical characteristics of

* Corresponding author.
*E-mail address:* vanessa.markwitz@research.uwa.edu.au (V. Markwitz).
Peer-review under responsibility of China University of Geosciences (Beijing).

http://dx.doi.org/10.1016/j.gsf.2017.04.004

the original source region over transportation distances. To evaluate this question, we investigate how the detrital zircon grain morphology correlates with its isotopic age and chemical composition. As one might expect, the extent to which a loss of grain shape similarity between source and sink can occur depends on whether or not grain shapes are heavily modified during transportation.

An important factor in consideration of detrital zircon populations is the likely zircon fertility of the source terrane. Zircon fertility encapsulates the concept that different quantities of zircon will grow within magmatic or metamorphic source rocks of favorable composition, e.g. enriched in Zr. Igneous mafic melts, for example, produce substantially less zircon crystals than felsic granitic melts (Moecher and Samson, 2006). However, even in felsic melts, zircon fertility is highly variable, depending on melt inheritance and recycling processes as well as new zircon precipitation (Watson and Harrison, 1983; Boehnke et al., 2013).

Numerous studies have argued that the global detrital record may be biased through selective preservation and that age spectra reflect episodic crustal reworking or growth events rather than being a function of the preservation potential and fertility of the original melt (e.g. Hawkesworth et al., 2009; Spencer et al., 2013; Parman, 2015; Roberts and Spencer, 2015). Zircon crystals are destroyed under specific chemical conditions such as dissolution in $CO_2$-rich waters (Carroll, 1953), supergene accumulations of organic matter, weathering and hydrothermal solution transfer (Balan et al., 2001). Mechanical failure can occur in crystals that were damaged or weakened by radiation from α-decay of U and Th isotopes (Murakami et al., 1991). The degree of metamictization leads to structural damage and grains are characterized by a decrease in density and hardness (Ewing et al., 2003). Grain shape surface textures are also related to the degree of radiation damage and grain shapes vary from euhedral well preserved crystals to well-rounded grains (Balan et al., 2001). Zircon crystals eroded from Archean granitic terranes may yield high proportions of metamict grains, which are more prone to be destroyed during detrital transport, diagenetic processes and weathering (Balan et al., 2001; Fedo et al., 2003; Hay and Dempster, 2009). During detrital transport, grains are sorted based on hydraulic behavior, controlled by grain size, density and shape (e.g. Schuiling et al., 1985; Komar, 2007). Higher densities and smaller grain sizes in heavy minerals result in lower transport rates when carried as part of the bedload or in suspension due to differences in settling velocities (Komar, 2007). Distributions of heavy minerals in sediments are further controlled by different depositional environments and mode of transport (Garzanti et al., 2009).

Zircons released from source rocks are sorted during transport based on their durability and density, which results in sediments that may contain a wide range of different grain morphologies (Garzanti et al., 2008; Kirkland et al., 2013). The primary morphology of magmatic zircon grains is determined by crystal habit, influenced by the relative growth-rates of pyramidal and prismatic crystal faces, and surface textures such as pitting and abrasion. Previous studies of zircon morphology have proposed that the predominance of {100} and {110} prisms is controlled by temperature and composition of the magma they crystallized from (Pupin, 1980). Using internal textures such as growth zonation produced during crystallization, Vavra (1990) and Vavra et al. (1999) concluded that the relative size relations of the main crystal faces {100} and {110} depend on the fluctuation of zirconium concentrations in the melt. The growth of these crystal faces correspond to the difference in zircon saturation in the melt, e.g., a decrease in zircon saturation is represented by low {110} growth rates relative to {100} and an increase in zircon supersaturation leads to preferential growth of {110} relative to {100} (Vavra, 1990). Whereas the morphologies of the pyramids {211} and {101} are determined by trace element substitution. Benisek and Finger (1993) reported that U content has a growth blocking effect on {110} and {100} prisms, postulating that low U content in granitic melts produce zircon grains with large prisms. Fluid induced processes such as metasomatism and metamorphism also strongly influence zircon grain shapes, and result in sub-rounded to irregular shaped xenocrystic zircons formed by overgrowth and corrosion in oversaturated environments (Corfu and Ayres, 1984; Corfu et al., 2003). In highly fractionated zircon saturated magmas the occurrence of fragmented and broken crystals appears common, controlled by the remaining pore space at late stage crystallization (Poldervaart, 1956; Scoates and Chamberlain, 1995; Corfu et al., 2003). These variable crystal morphologies should be reflected in the grain shapes that are routinely imaged for *in situ* geochronology, and depending on transport processes, may survive from the original growth environment to the depositional site.

Relationships between magmatic source rocks and detrital zircon populations are important to help constrain sedimentary recycling pathways. Transport of detritus in a fluvial environment is dependent on the fluctuation rate of an active river system, therefore hydraulic sorting and mechanical abrasion within sediments determines relationships between grain density, shape and grain size (Garzanti et al., 2008). In aeolian transport detrital minerals are likely to be rounded by mechanical abrasion, whereas in tidal to marine environments, roundness of grains appears to decrease relative to aeolian transport settings (Garzanti et al., 2015). Concentrations of more dense grains are systematically found in fine-grained sedimentary fractions. Furthermore, Lawrence et al. (2011) has shown that hydraulic sorting of detrital zircons in sediments can, on occasion, lead to correlation between grain size and age. There have been attempts made to correlate magmatic zircon morphology with changes in trace elements based on the classification by Pupin (1980) and individual morphological characteristics have been related to petrogenetic processes, such as magma mixing and evolution in specific S- and I-type granitoids (Belousova et al., 2006).

Numerous approaches for grain measurements exist, including Fourier series analysis on digitized 2D grain outlines to describe roundness and textures (e.g. Ehrlich and Weinberg, 1970; Mazzullo and Ehrlich, 1983; Barclay and Buckingham, 2009), fractal analysis of size and texture (e.g. Hyslip and Vallejo, 1997), 2D crystal size measurements based on digitized images (e.g. Simigian and Starkey, 1986; Morgan and Jerram, 2006; Cox and Budhu, 2008), wavelet analysis to determine grain size distributions (Buscombe, 2013) and visual classification schemes for heavy minerals based on microscope images (Andò et al., 2012). In this contribution we use an automated approach to obtain grain sizes and a diversity of different grain shape descriptors based on digitized two dimensional grain sections using the ImageJ software.

Sediments usually contain biased erosional records due to the different susceptibility of source rocks to erosion. The link between source rocks and sediments depends on erosion laws (Allègre and Rousseau, 1984) expressed in the calculation of the erosion parameter '*K*', which determines the proportion of source detritus that is lost during transportation compared to the proportion in the catchment area. Dhuime et al. (2011) studied *K* based on U–Pb and Hf isotopes in detrital zircon grains. We expand the calculation of *K* based on U–Pb ages with *K* based on grain shape, an association which has not been quantitatively assessed before. Here we combine image analysis of digitized sections of zircon grains with multiple linear regression modeling to quantify whether or not the correlation between grain shapes, apparent lattice damage based on calculated alpha dose and U and Th concentrations are statistically significant for both detrital and magmatic zircon grains. We

apply this approach to examine source–sink relationships in two well characterized source regions in terms of detrital transport systems, regional geology and sedimentation ages in Western Australia for which an extensive dataset of secondary ionization mass spectrometry (SIMS) U–Pb dated zircons already exists (data package: Geological Survey of Western Australia, 2016). Study region (1) comprises Archean basement rocks and their associated Paleoproterozoic metasedimentary rocks along the northern margin of the Yilgarn Craton, and study region (2) includes Mesoproterozoic basement rocks of the Musgrave Province and their related Neoproterozoic metasedimentary rocks of the Amadeus Basin (Fig. 1). We assess the preservation bias within the detrital zircon record by evaluating the extent to which selective destruction processes such as the removal of metamict zircon grains may bias the detrital zircon record. To evaluate this potential bias in the detrital zircon record we compare magmatic zircon crystals with multiple-cycle detrital zircon grains using the grains morphological and chemical characteristics. By applying this approach across all samples, we are able to show quantitatively that zircon grain shape/age distributions are still strongly linked to their origin, despite hydraulic sorting during transport.

## 2. Sample descriptions and geological setting

Two different well-characterized sample areas (Fig. 1A) were chosen to evaluate if statistically significant relationships between zircon morphology, age, trace element composition and whole rock geochemistry exist. Samples were subject to an established heavy mineral processing routine and SIMS dating as detailed in Geological Survey of Western Australia (2016). In study region (1) we have chosen sample locations from thirteen different magmatic rocks located predominantly in Archean granites of the Narryer Terrane including the Yarlarweelor Gneiss Complex (northern Yilgarn Craton) and nine metasedimentary samples from Paleoproterozoic arenites, mudstones, shales and metasandstones of Capricorn Orogen basins to characterize the sink region (Table 1; Fig. 1B). For study region (2) twelve sample locations were available, including eight Mesoproterozoic granite samples from the Mount Aloysius Complex in the western part of the Musgrave Province, as well as the Umutju Granite (Pitjantjatjara Supersuite), Giles Complex, and the Musgrave Gneiss. To characterize the sink region four metasedimentary samples were available from the Meso–Neoproterozoic western part of the Amadeus Basin in Western Australia (Table 1; Fig. 1C).

### 2.1. Study region (1): Northern Yilgarn Craton and Capricorn basins

The Archean Yilgarn Craton consists of gneisses, metasedimentary and metavolcanic successions, and granites, and has been divided into several tectonic units. The northern part of the Yilgarn Craton consists, from west to east of the Narryer Terrane, the Youanmi Terrane, and the Eastern Goldfields Superterrane (Fig. 1B). The ca. 3.7–2.6 Ga Narryer Terrane is dominated by granitoids and high-grade gneisses, including one of the oldest rocks on Earth, the 3.7 Ga Meeberrie gneiss (Kinny and Nutman, 1996) and also the location of Earth's oldest detrital zircon with an age of ca. 4.44 Ga from a conglomerate at Jack Hills (Wilde et al., 2001; for location see Fig. 1B). The Narryer Terrane also includes the Yarlarweelor Gneiss Complex, an Archean gneiss complex within the Capricorn Orogen. The ca. 3.0–2.6 Ga Youanmi Terrane comprises N-trending elongated greenstone belts and extensive areas of granites and gneisses, while the Eastern Goldfields Superterrane contains distinct N–NW trending greenstone belts ranging in ages between 2.9 Ga and 2.6 Ga.

Archean rocks of the Yilgarn Craton are known to be the major sources for metasedimentary rocks in the Capricorn Orogen, where four major basins record periods of sedimentation, volcanism, rifting, accretion, and passive-margin formation (Johnson, 2013). All Paleoproterozoic basins, including the ca. 2.2 Ga Yerrida Basin, the ca. 2.0 Ga Bryah Basin, the 1.98–1.81 Ga Padbury Basin, and ca. 1.84 Ga Earaheedy Basin (Pirajno and Adamides, 2000; Pirajno and Occhipinti, 2000) overly Archean rocks of the Yilgarn Craton or associated inliers. Additionally, all four basins were deformed and metamorphosed during the 1.82–1.77 Ga Capricorn Orogeny (Sheppard et al., 2003).

On top of the Archean basement, sediments of the Windplain Group were deposited in the intracratonic Yerrida Basin, comprising siliciclastic sediments, carbonates and evaporites (Pirajno et al., 2004). These sediments were overlain by thick layers of shales, which were then disconformably overlain by turbidites and basalts of the Mooloogool Group (including Killara Formation) (Pirajno and Occhipinti, 2000). To the west of the Yerrida Basin the Earaheedy Basin developed in a passive margin setting on top of the Archean Yilgarn Craton. The Earaheedy Basin rests unconformably on Archean rocks of the Yilgarn Craton and on deformed Paleoproterozoic rocks of the Yerrida Basin and contains a 5 km thick shallow marine clastic and chemical sedimentary succession of the Earaheedy Group, in which the Mount Leake Formation marks the tectonic boundary between Bryah and Yerrida basins (Pirajno et al., 2009). The Bryah Basin contains volcano-sedimentary sequences of the Bryah Group, which consists amongst others of the Ravelstone Formation comprising turbidites, argillites and ironstones. All sequences were deformed and metamorphosed to greenschist facies conditions (Pirajno et al., 2004). The Padbury Basin developed as a foreland basin on top of the Bryah Basin, containing clastic and chemical sedimentary rocks of the Padbury Group in which the Wilthorpe Formation belongs to the lower part of this Group, amongst other members. The Wilthorpe Formation evolved as an upward-coarsening succession of turbidites.

The Badgeradda Basin is part of the Proterozoic Pinjarra Orogen adjacent the northwestern Yilgarn Craton, comprising basal sandstone beds of the Bililly Formation (Perry and Dickins, 1960) and within the Youanmi Terrane itself. This sandstone-siltstone succession was probably deposited during the late Proterozoic and subsequently intruded by dykes and sills (Perry and Dickins, 1960).

Further details on the geological evolution of the Northern Yilgarn Craton and Capricorn basins are given in Nelson (2001), Rasmussen and Fletcher (2002), Muhling et al. (2012), Rasmussen et al. (2012), Johnson (2013), Hawke et al. (2015), and Sheppard et al. (2016) and need not be reiterated here.

### 2.2. Study region (2): Musgrave Province and Amadeus Basin

The West Musgrave Province consists of an E–W trending Meso- to Neoproterozoic belt dominated by granites, which experienced three major orogenic events: (1) the 1.34–1.29 Ga Mount West Orogeny produced the Wankanki Supersuite calc-alkaline magmatism, likely a response to amalgamation of the three Australian Proterozoic cratons, West – North – South; (2) the 1.22–1.15 Ga Musgrave Orogeny dominated by alkali-calcic magmatism of the Pitjantjatjara Supersuite; and (3) the 1.08–1.03 Ga Giles Event with the intrusion of giant mafic-ultramafic bodies (Wade et al., 2008; Smithies et al., 2011; Johnson, 2013; Howard et al., 2015). The intracratonic Amadeus Basin is bounded by the Musgrave Province to the south and the Arunta Orogen to the north (Fig. 1A, C), exposing Paleoproterozoic to early Paleozoic rocks (Collins and Shaw, 1995; Hand et al., 1999; Buick et al., 2001; Scrimgeour et al., 2005; Haines et al., 2008, 2012). Both crystalline basement terranes are believed to be the source regions for the basal sediment sequences within the Amadeus Basin (Zhao et al., 1992). The Amadeus Basin is a Mesoproterozoic to early Phanerozoic basin in central Australia with

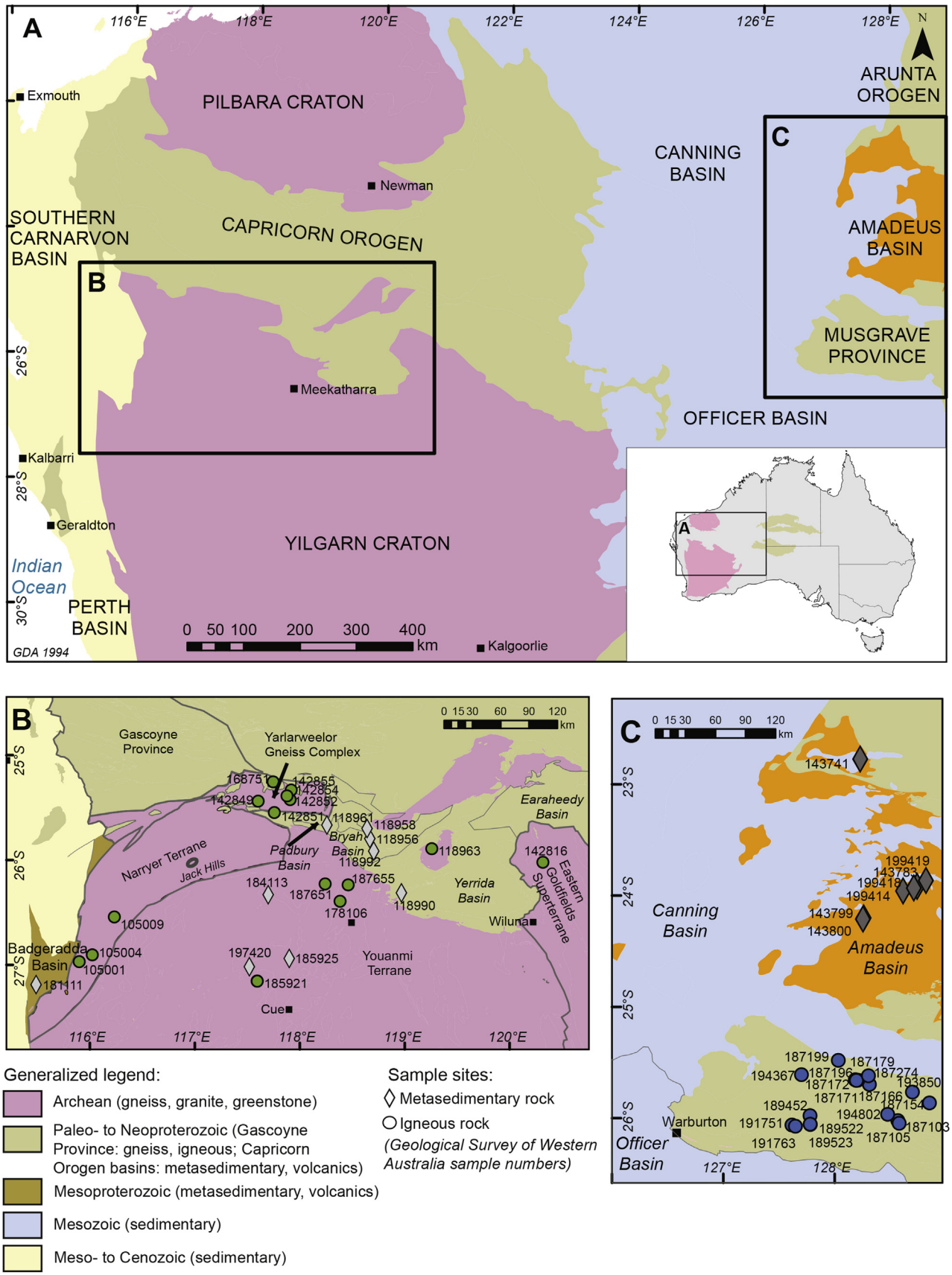


**Figure 1.** Overview map (A) showing the location of both study regions in Western Australia: generalized geological maps including sample locations for the northern Yilgarn Craton/Capricorn basins region (B) and for the Musgrave Province/Amadeus Basin region (C).

**Table 1**
Sample summary with short lithological descriptions and ages of both study regions: northern Yilgarn Craton/Capricorn basins and Musgrave Province/Amadeus Basin.

| | | Sample ID | Dlat (S)/Dlong (E) | $^{207}Pb/^{206}Pb$ age (Ma) | Lithology | Tectonic unit/unit name |
|---|---|---|---|---|---|---|
| Study region (1) | Northern Yilgarn Craton | 105004.1 | 26.90481°/116.0239° | 2638 ± 6 | Late monzogranite | Narryer Terrane |
| | | 105001.1 | 26.96982°/115.8994° | 2683 ± 4 | Late-tectonic, recrystallized, coarse-grained monzogranite | Narryer T./Yallalong Granite |
| | | 105009.1 | 26.545°/116.2336° | 3495 ± 3 | Dark inclusion within leucocratic orthogneiss | Narryer T. |
| | | 118963.1 | 25.89294°/199.2587° | 2624 ± 8 | Porphyritic syenogranite | Youanmi T., Goodin Inlier |
| | | 142816.1 | 26.02183°/120.3175° | 2648 ± 19 | Undeformed biotite monzogranite | Goldfields T. |
| | | 142852.1 | 25.42382°/117.9092° | 1797 ± 4 | Recrystallized monzogranite dyke | Narryer T., Yarlarweelor Gneiss Complex |
| | | 142854.1 | 25.38888°/117.8788° | 1811 ± 9 | Medium-grained, weakly foliated granite dyke | Narryer T., Yarlarweelor Gneiss Complex |
| | | 142855.1 | 25.33265°/117.9191° | 1619 ± 15 | Medium-grained, porphyritic monzogranite pluton | Narryer T., Yarlarweelor Gneiss Complex |
| | | 168751.1 | 25.25506°/117.7468° | 1644 ± 6 | Xenolith (20 m × 50 m) of fine- to medium-grained biotite monzogranite | Narryer T., Yarlarweelor Gneiss Complex |
| | | 178106.1 | 26.384222°/118.3781° | 2744 ± 4 | Porphyritic andesite, part of the Abbotts greenstone belt | Murchison Domain, Youanmi T., Yilgarn C. |
| | | 185921.1 | 27.15349°/117.595° | 2757 ± 4 | Strongly foliated, K-feldspar and quartz porphyritic monzogranite | Murchison Domain, Youanmi T., Yilgarn C. |
| | | 187651.1 | 26.22814°/118.2427° | 2650 ± 4 | Biotite monzogranite | Murchison Domain, Youanmi T., Yilgarn C. |
| | | 187655.1 | 26.23795°/118.4616° | 2643 ± 4 | Biotite monzogranite | Murchison Domain, Youanmi T., Yilgarn C. |
| | Capricorn Basins | 118956.1 | 25.79373°/118.6677° | 1785 ± 11 | Well-sorted, pale greenish-grey, glauconite-bearing sandstone | Bryah B./Ravelstone F. (Bryah Group) |
| | | 118958.1 | 25.69934°/118.641° | 2014 ± 22 | Poorly sorted, muscovite-bearing immature sandstone | Bryah B./Ravelstone F. (Bryah Group) |
| | | 118961.1 | 25.66552°/118.2589° | 1996 ± 35 | Coarse-grained fragmental mudstone | Padbury B./Wilthorpe F. (Padbury Group) |
| | | 118990.1 | 26.31288°/118.9683° | 1764 ± 13 | Silicified laminated shale | Yerrida B./Killara F. (Yerrida Group) |
| | | 118992.1 | 25.91409°/118.7044° | 1832 ± 37 | Well-sorted fine-grained quartz sandstone | Earaheedy Basin/Mount Leake Formation |
| | | 181111.1 | 27.18672°/115.4875° | 1173 ± 6 | Silicified, cross-bedded, well sorted quartz sandstone to quartzite | Badgeradda B.(Pinjarra Orogen); Bililly F. |
| | | 184113.1 | 26.33059°/117.6992° | 2638 ± 6 | Quartz sandstone | Murchison Domain, Youanmi T., Yilgarn C. |
| | | 185925.1 | 26.93812°/117.8999° | 2740 ± 4 | Andalusite-rich quartzite | Murchison Domain, Youanmi T., Yilgarn C. |
| | | 197420.1 | 27.01629°/117.5191° | 2728 ± 11 | Silicified and hematized lithic quartz metasandstone | Murchison Domain, Youanmi T., Yilgarn C. |
| Study region (2) | Musgrave Province | 187103.1 | 26.02275°/128.5684° | 1191 ± 4 | Medium-grained leucogranitic, garnetiferous leucogranite | Musgrave Province/Mount Aloysius C. |
| | | 187105.1 | 26.04724°/128.5807° | 1190 ± 7 | Medium-grained leucogranite | Musgrave Province/Mount Aloysius C. |
| | | 187154.1 | 25.86383°/128.8527° | 1185 ± 10 | Mafic granulite | Musgrave Province/undefined |
| | | 187171.1 | 25.65496°/128.1869° | 1185 ± 5 | Charnockitic syenogranite | Musgrave Province/Umutju Granite |
| | | 187172.1 | 25.64621°/128.1864° | 1212 ± 56 | Coarse-grained, leucocratic, granite pegmatite | Musgrave Province/Pitjantjatjara Supersuite |
| | | 187196.1 | 25.66124°/128.1969° | 1200 ± 5 | Leucogranite | Musgrave Province/Umutju Granite, Pitjantjatjara S. |
| | | 187199.1 | 25.48075°/128.0336° | 1193 ± 6 | Dacite | Musgrave Province/Giles C., Pitjantjatjara Supersuite |
| | | 191763.1 | 26.07354°/127.6491° | 1134 ± 9 | Granitic pegmatite dyke | Musgrave Province/Musgrave Gneiss |
| | Amadeus Basin | 143783.1 | 23.91655°/128.7417° | 820 ± 13 | Quartz-rich, fine to medium-grained sandstone | Amadeus B., Centralian Superbasin/ Carnegie F. |
| | | 143800.1 | 24.2096°/128.2546° | 1059 ± 8 | Fine- to coarse-grained lithic quartz sandstone | Amadeus B., Centralian Superbasin/Ellis Sandstone |
| | | 199414.1 | 23.95802°/128.6154° | 698 ± 20 | Medium-grained, poorly sorted, lithic-feldspathic sandstone | Amadeus B., Centralian Superbasin/Maurice F. |
| | | 199418.1 | 23.93103°/128.7115° | 1059 ± 57 | Fine-grained, quartz-lithic sandstone | Amadeus B., Centralian Superbasin |

multiple tectono-stratigraphic events separated by distinct unconformities (Shaw et al., 1991). Basin formation at ca. 800 Ma is interpreted to be related to the mid-Proterozoic breakup of Rodinia with sag basin development (Lindsay et al., 1987). At the onset of subsidence typical basal sandstones of the Neoproterozoic Heavitree Quartzite were deposited throughout the basin (Lindsay, 1999). These sediments are equivalent to the Kulail Sandstone and Dean Quartzite in the south-western part of the Amadeus Basin in Western Australia (Haines et al., 2008; Fig. 1C). The basal quartzites are overlain by the Neoproterozoic Bitter Springs Formation, which is then unconformably overlain by the thick siliciclastic sequences of the Neoproterozoic to Early Cambrian Ellis Sandstone, Sir Frederick Conglomerate, Maurice Formation and Carnegie Formation. The Carnegie Formation has been interpreted to be deposited in a foreland basin setting related to the 580–530 Ma Petermann Orogeny (Haines et al., 2012). The detailed geological evolution of this study region is described in Haines et al. (2001, 2008, 2016), Wade et al. (2008), Smithies et al. (2011), Camacho et al. (2015) and Howard et al. (2015).

## 3. Methods

Sample preparation and mineral separation by the Geological Survey of Western Australia followed a comparable process for each sample (Geological Survey of Western Australia, 2016): (1) Rock fragments were ground to a powder and passed through a sieve with a 400 μm mesh size; (2) the remaining fraction was passed through heavy liquids (aqueous sodium polytungstate solution) to obtain a heavy mineral concentrate; (3) highly magnetic minerals were removed using hand magnet, followed by a Frantz magnetic

barrier separator; (4) the removal of less dense minerals was accomplished by placing the processed fraction in methylene iodide; (5) crystals were handpicked under a binocular microscope from this processed material; (6) the grains were aligned in rows, oriented parallel to zircon prism faces and then mounted in 25 mm diameter epoxy resin disks; (7) finally epoxy mount surfaces were polished to half grain thickness to expose grain interiors.

Both the collection and presentation of age data from heavy minerals are vulnerable to subjective bias, including preferential selection of grains during handpicking and during selection of the analysis location. Further bias may be introduced through magnetic separation (Sircombe, 2000; Sircombe and Stern, 2002).

In this work grain shape descriptors are presented for crystals that have published U–Pb geochronology (see: http://dmp.wa.gov.au/geochron/). In short, the geochronology procedure involved using the sensitive high-resolution ion microprobe (SHRIMP II) at the John de Laeter Centre (Curtin University). U–Pb dates are filtered for concordance at a 10% discordance threshold and normalized probability density plots of samples are provided to illustrate the age spectra of relevant samples (Fig. 6). Dates younger than 1000 Ma are calculated based on the $^{238}U/^{206}Pb$ ratio and ages older than 1000 Ma are based on the $^{207}Pb/^{206}Pb$ ratio.

Whole rock geochemistry is available for the examined samples from the GSWA geochemistry data base (WACHEM; http://geochem.dmp.wa.gov.au/geochem/).

### 3.1. Image processing and statistical correlation of zircon grain shapes with age and U and Th content

We quantified the two-dimensional shape characteristics of 819 zircon grains from 34 sample sites by using cathodoluminescence images of separated zircon grains in polished epoxy mounts. We screened all zircon images to avoid irregular cut effects and ignored grains that appeared to not be oriented parallel to the c-axis to ensure that cross-sections of the most representative crystals from each sample were measured. Zircon images were analyzed using ImageJ

**Table 2**
Definitions of shape descriptor dimensions used in ImageJ (after Russ, 2002; Abramoff et al., 2004; Syverud et al., 2007; Schneider et al., 2012) to describe shape characteristics of sectioned zircon grains.

| ImageJ measure | Description | ImageJ measure | Description |
|---|---|---|---|
| Aspect Ratio (AR) | AR = Major Axis/Minor Axis; ratio of width (shorter axis) to length (along c-axis) and represents the irregularity of the grain | Perimeter (P) | The perimeter is calculated per the Cauchy-Crofton equation, from the number of intercepts formed by a series of parallel lines, with spacing, exploring N directions, and from $\alpha$ to $\pi$. |
| Circularity (Ci) | $Ci = 4\pi$ (Area/Perimeter)$^2$; combines the surface area expression and symmetry of the contour | Major Axis (MaA) | Replaces an area selection with the best fit ellipse (same area, orientation and centroid as original particle); major length is measured |
| Compactness (Cc) | $Cc = (4/\pi)$ (Area)$^2$/Major Axis; curvature measure | Minor Axis (MiA) | Replaces an area selection with the best fit ellipse (same area, orientation and centroid as original particle); minor length is measured |
| Roundness (Rn) | $Rn = 4 \times$ Area/$\pi$ (Major Axis)$^2$; a measure of the difference between grain surface contour expression and a circular surface, with a maximum Feret diameter | Form Factor (Ff) | $Ff = 4\pi \times$ Area/Perimeter$^2$ |
| Solidity (S) | S = Area/convex hull area; describes the convexity of the polygon that defines the contour of the surface area | Area (A) | The area is calculated as the sum of the areas of each individual pixel within the contour of the grain |
| Effective Diameter (ED) | ED = (Area/$\pi$)$^2$; approximation of the grains surface area contour to a sphere, averaged by the maximum and minimum diameter | | |

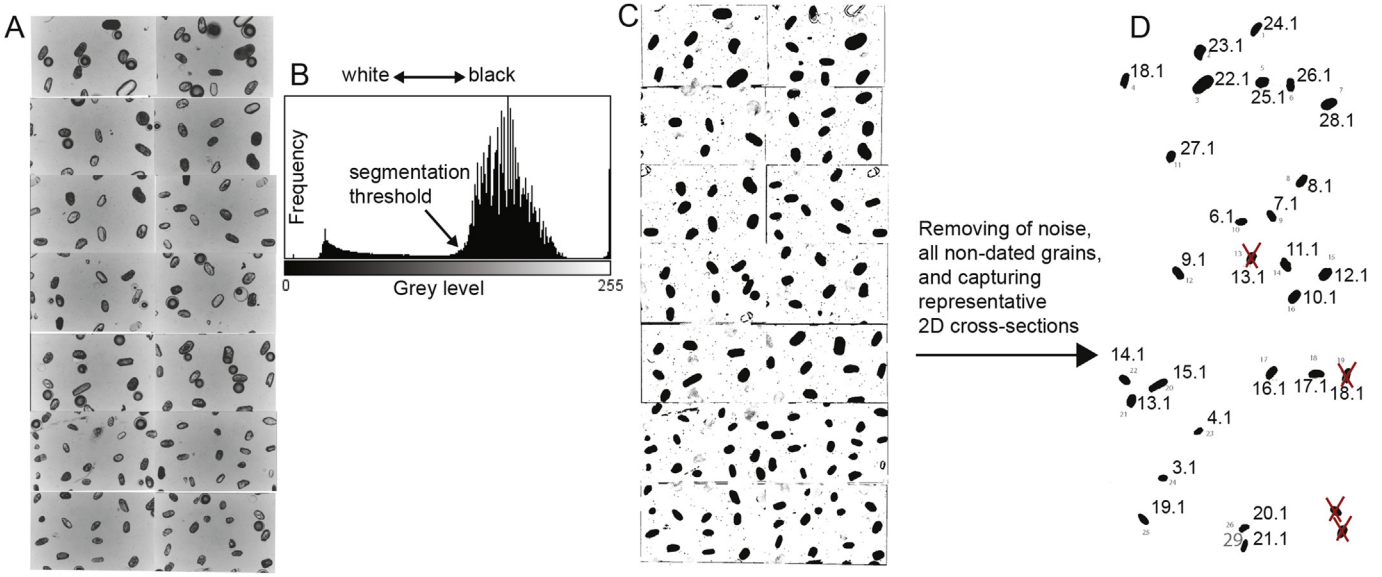


**Figure 2.** Illustration of image processing analysis from selected zircon sample. (A) Grey-scale image of separated scaled zircons; (B) segmentation threshold based on binarization histogram; (C) binarized image of zircon grains; (D) selection of U–Pb dated zircons and labeling.

**Table 3**
General statistics on zircon *Minor Axis* measurements (STD: standard deviation).

| | | Zircon type | Minor axis (μm) | |
|---|---|---|---|---|
| Study region (1) | Northern Yilgarn Craton | Magmatic | 42–353 | Range |
| | | | 137 | Mean |
| | | | 124 | Median |
| | | | 68 | STD |
| | Capricorn basins | Detrital | 44–673 | Range |
| | | | 162 | Mean |
| | | | 109 | Median |
| | | | 122 | STD |
| Study region (2) | Musgrave Province | Magmatic | 60–425 | Range |
| | | | 159 | Mean |
| | | | 137 | Median |
| | | | 75 | STD |
| | Amadeus Basin | Detrital | 78–285 | Range |
| | | | 143 | Mean |
| | | | 139 | Median |
| | | | 34 | STD |

software (Abramoff et al., 2004; Schneider et al., 2012), including the "Shape Descriptor1u" plugin (Syverud et al., 2007) to quantify grain sizes and shapes (see Table 2). Zircon grain shape analysis included two basic morphological image-based modeling operations such as the dilation/erosion method accompanied by the opening/closing operations (Serra, 1982). The opening operation is defined as erosion followed by dilation, which removes bright features such as ridges and captures the grains outline, while closing is defined by dilation followed by erosion and fills in dark regions, capturing the grains inside. Where dilation is defined as a maximum operator and selects the brightest value in the neighborhood of an individual grain by a certain threshold value, erosion represents the darkest value in a neighborhood. The transformed image was simplified in the morphological processing, which makes it possible to measure and quantify grain shapes and sizes. Binarization of the grey scale images, based on global thresholding of single grey scale values was performed in order to separate grains from each other (Fig. 2). A watershed segmentation algorithm using flooding simulations was used to separate touching grains (Soille and Vincent, 1990). Twelve different shape descriptors were measured to characterize zircon grain shapes, including *Aspect Ratio*, *Circularity*, *Compactness*, *Roundness*, *Solidity*, *Effective Diameter*, *Perimeter*, *Major Axis*, *Minor Axis*, *Form Factor*, and *Area* (Table 2; Appendix A1).

To investigate statistical significance and quantitative characterization of apparent relationships between all measured shape factors, zircon ages and their U and Th concentrations, we performed multiple linear regression analysis. For this, we assumed that in the linear regression model (lm) the data was independent and normally distributed with zero mean and constant variance. Dependent variables in this model are $^{206}Pb/^{207}Pb$ ages, U and Th concentrations, which are applied to the 'lm function'. To test the statistical hypothesis from the computed F-statistics, in which each dataset was tested against the null hypothesis ($\beta = 0$), we calculated the p-value with a threshold value of $\leq$0.05. A list of significant test results is given in Table 4. Data coverage, quality and how well the data fit the statistical model are expressed by the adjusted $R^2$ value (Table 4).

### 3.2. Statistical correlation between zircon grain shape and whole rock geochemistry

Whole rock geochemistry data in magmatic rocks from the Northern Yilgarn Craton and the Musgrave Province was examined to test for correlations between whole rock chemistry (major

**Table 4**
Statistical significance test (p-values) and adjusted $R^2$ values of zircon shape factors and their relationship to age and chemistry.

| | $^{207}Pb/^{206}Pb$ (age) | | $^{238}U$ (ppm) | | $^{232}Th$ (ppm) | | $^{232}Th/^{238}U$ | | $n^a$ |
|---|---|---|---|---|---|---|---|---|---|
| | Significant shape descriptor | p-values | Significant shape descriptor | p-values | Significant shape descriptor | p-values | Significant shape descriptor | p-values | |
| **(1) Northern Yilgarn Craton, Capricorn basins** | | | | | | | | | |
| Magmatic rocks | *Compactness* | 0.000966 | ***Minor Axis*** | **3.10E-09** | *Minor Axis* | 0.00328 | *Area* | 0.00742 | 226 |
| | *Form Factor* | 0.008838 | *Eff. Diameter* | 9.02E-08 | *Area* | 0.00971 | *Major Axis* | 0.00354 | |
| | *Solidity* | 0.007085 | *Form Factor* | 3.07E-07 | *Solidity* | 0.00536 | *Minor Axis* | 0.00301 | |
| | ***Minor Axis*** | **0.005931** | *Compactness* | 0.00071 | *Compactness* | 0.00208 | *Solidity* | 0.00572 | |
| | ***Eff. Diameter*** | **0.001694** | | | *Eff. Diameter* | 0.00624 | *Form Factor* | 0.01853 | |
| | *Major Axis* | 0.012732 | | | *Form Factor* | 0.01342 | *Compactness* | 0.00129 | |
| | *Area* | 0.017846 | | | *Major Axis* | 0.011 | *Eff. Diameter* | 0.00354 | |
| | Adjusted $R^2$ | 0.377 | | 0.339 | | 0.369 | | 0.376 | |
| Meta-sedimentary rocks | ***Eff. Diameter*** | **4.20E-14** | *Roundness* | 3.12E-08 | *Area* | 2.01E-06 | *Area* | 1.80E-06 | 300 |
| | ***Minor Axis*** | **1.25E-08** | ***Eff. Diameter*** | **6.66E-07** | *Major Axis* | 4.50E-10 | *Major Axis* | 4.79E-10 | |
| | *Circularity* | 5.29E-06 | *Area* | 7.67E-07 | *Circularity* | 8.94E-07 | *Circularity* | 7.63E-07 | |
| | *Area* | 1.27E-05 | *Circularity* | 2.85E-06 | *Roundness* | <2e-16 | *Roundess* | <2e-16 | |
| | *Solidity* | 0.000103 | *Solidity* | 1.08E-05 | *Solidity* | 7.52E-06 | *Solidity* | 8.29E-06 | |
| | *Roundness* | 0.000765 | *Major Axis* | 6.76E-05 | *Eff. Diameter* | 6.88E-07 | | | |
| | | | ***Minor Axis*** | **4.32E-02** | | | | | |
| | Adjusted $R^2$ | 0.594 | | 0.602 | | 0.586 | | 0.584 | |
| | ***Minor Axis***, *Eff. Diameter* | | ***Minor Axis***, *Eff. Diameter* | | *Eff. Diameter, Area* | | *Area* | | 526 |
| **(2) Musgrave Province, Amadeus Basin** | | | | | | | | | |
| Magmatic rocks | *Perimeter* | 1.51E-07 | *Perimeter* | 1.35E-03 | *Perimeter* | 7.68E-08 | *Perimeter* | 6.47E-11 | 161 |
| | ***Minor Axis*** | **0.04104** | *Major Axis* | 4.24E-02 | | | *Solidity* | 0.002188 | |
| | *Solidity* | 0.001138 | ***Minor Axis*** | **4.14E-02** | | | *Eff. Diameter* | 0.000866 | |
| | *Eff. Diameter* | 0.000126 | *Solidity* | 0.00207 | | | | | |
| | | | ***Eff. Diameter*** | **0.00528** | | | | | |
| | Adjusted $R^2$ | 0.395 | | 0.234 | | 0.279 | | 0.310 | |
| Meta-sedimentary rocks | *Area* | 2.38E-08 | *Area* | 1.09E-05 | *Area* | 1.87E-08 | *Area* | 3.86E-08 | 132 |
| | ***Minor Axis*** | **1.32E-02** | ***Minor Axis*** | **4.26E-02** | *Form Factor* | 1.63E-02 | *Form Factor* | 1.97E-02 | |
| | | | *Form Factor* | 4.36E-02 | *Eff. Diameter* | 3.46E-07 | *Eff. Diameter* | 4.72E-07 | |
| | | | ***Eff. Diameter*** | **3.70E-07** | | | | | |
| | Adjusted $R^2$ | 0.233 | | 0.278 | | 0.270 | | 0.253 | |
| | ***Minor Axis*** | | ***Minor Axis***, *Eff. Diameter* | | *N/A* | | *Eff. Diameter* | | 293 |

[a] Number of observations (out of 18 variables); most consistent shape factor are noted in bold typeface and ImageJ measures in italic typeface.

**Table 5**
Pearson's correlation coefficient results between whole rock geochemistry data and *Minor Axis*/*Effective Diameter* shape descriptors for (A) major elements (in wt.%) and (B) rare earth elements (REE, in ppm) in both study areas. Highly correlated values are represented in bold.

(A)

| | $Al_2O_3$ | CaO | $K_2O$ | $Na_2O$ | $SiO_2$ | $Na_2O + K_2O$ | Zr | Th/U | Per-aluminous | *Eff. Diameter* | *Minor Axis* |
|---|---|---|---|---|---|---|---|---|---|---|---|
| Study area (1): Northern Yilgarn Craton | | | | | | | | | | | |
| $Al_2O_3$ | 1.000 | 0.584 | **−0.913** | **0.980** | −0.866 | −0.553 | −0.644 | −0.439 | **0.958** | −0.432 | −0.280 |
| CaO | 0.583 | 1.000 | −0.818 | 0.491 | −0.475 | −0.982 | 0.069 | 0.455 | 0.730 | 0.132 | −0.563 |
| $K_2O$ | **−0.913** | −0.818 | 1.000 | −0.895 | 0.676 | 0.829 | 0.504 | 0.132 | **−0.988** | 0.071 | 0.598 |
| $Na_2O$ | **0.980** | 0.491 | −0.895 | 1.000 | −0.768 | −0.493 | −0.777 | −0.551 | **0.951** | −0.340 | −0.366 |
| $SiO_2$ | −0.866 | −0.475 | 0.676 | −0.768 | 1.000 | 0.357 | 0.314 | 0.317 | −0.728 | 0.774 | −0.184 |
| $Na_2O + K_2O$ | −0.553 | **−0.982** | 0.829 | 0.493 | 0.357 | 1.000 | 0.011 | −0.432 | −0.737 | −0.287 | 0.707 |
| Zr | −0.644 | 0.069 | 0.504 | −0.777 | 0.314 | 0.011 | 1.000 | 0.867 | −0.603 | 0.129 | 0.350 |
| Th/U | −0.439 | 0.455 | 0.132 | −0.551 | 0.173 | −0.432 | 0.867 | 1.000 | −0.273 | 0.456 | −0.148 |
| Peraluminous | **0.958** | 0.730 | **−0.988** | **0.951** | −0.728 | −0.737 | −0.603 | −0.273 | 1.000 | −0.169 | −0.529 |
| *Eff. Diameter* | −0.367 | −0.531 | 0.645 | −0.465 | −0.115 | 0.676 | 0.473 | −0.015 | −0.595 | 1.000 | **0.990** |
| *Minor Axis* | −0.280 | −0.563 | 0.598 | −0.366 | −0.184 | 0.707 | 0.350 | −0.148 | −0.529 | −0.743 | 1.000 |

| | $Al_2O_3$ | CaO | $K_2O$ | $Na_2O$ | $SiO_2$ | $Na_2O + K_2O$ | Zr | Th/U | Per-aluminous | *Eff. Diameter* | *Minor Axis* |
|---|---|---|---|---|---|---|---|---|---|---|---|
| Study area (2): Musgrave Province | | | | | | | | | | | |
| $Al_2O_3$ | 1.000 | **0.957** | −0.770 | 0.735 | **−0.901** | −0.727 | −0.262 | −0.497 | −0.067 | 0.025 | −0.316 |
| CaO | **0.957** | 1.000 | **−0.902** | 0.833 | **−0.951** | −0.865 | −0.233 | −0.502 | −0.057 | −0.099 | −0.242 |
| $K_2O$ | −0.770 | **−0.902** | 1.000 | −0.866 | 0.837 | **0.976** | 0.293 | 0.248 | −0.194 | 0.215 | 0.072 |
| $Na_2O$ | 0.735 | 0.833 | −0.886 | 1.000 | −0.886 | −0.765 | 0.045 | −0.458 | −0.119 | −0.004 | −0.360 |
| $SiO_2$ | **−0.901** | **−0.951** | 0.837 | −0.886 | 1.000 | 0.750 | −0.070 | 0.599 | 0.275 | −0.090 | 0.280 |
| $Na_2O + K_2O$ | −0.727 | −0.865 | **0.976** | −0.765 | 0.750 | 1.000 | 0.428 | 0.132 | −0.325 | 0.296 | −0.668 |
| Zr | −0.262 | −0.233 | 0.293 | 0.045 | −0.072 | 0.428 | 1.000 | −0.260 | −0.699 | 0.628 | −0.010 |
| Th/U | −0.497 | −0.502 | 0.248 | −0.458 | 0.599 | 0.132 | −0.260 | 1.000 | 0.828 | 0.199 | 0.766 |
| Peraluminous | −0.067 | −0.057 | −0.194 | −0.119 | 0.275 | −0.325 | −0.699 | 0.828 | 1.000 | −0.146 | 0.548 |
| *Eff. Diameter* | 0.025 | −0.099 | 0.215 | −0.004 | −0.095 | 0.296 | 0.629 | 0.199 | −0.146 | 1.000 | 0.286 |
| *Minor Axis* | −0.316 | −0.242 | 0.072 | −0.360 | 0.280 | −0.066 | −0.010 | 0.766 | 0.548 | 0.286 | 1.000 |

**(B)**

| | Ce | Dy | Er | Eu | Gd | Ho | La | Lu | Nd | Sc | Sm | Tb | Y | Yb | *Eff. Diameter* | *Minor Axis* |
|---|---|---|---|---|---|---|---|---|---|---|---|---|---|---|---|---|
| Study area (1): Northern Yilgarn Craton | | | | | | | | | | | | | | | | |
| Ce | 1.000 | 0.891 | 0.728 | 0.644 | **0.985** | 0.830 | **0.993** | 0.365 | **0.997** | 0.432 | **0.997** | **0.953** | 0.620 | 0.374 | −0.492 | **0.919** |
| Dy | 0.891 | 1.000 | **0.952** | 0.232 | **0.983** | **0.988** | 0.842 | 0.686 | 0.862 | 0.689 | **0.920** | **0.985** | **0.908** | 0.739 | −0.209 | 0.808 |
| Er | 0.728 | **0.952** | 1.000 | −0.052 | 0.823 | **0.986** | 0.670 | 0.870 | 0.691 | 0.674 | 0.770 | 0.892 | **0.974** | **0.907** | 0.083 | 0.595 |
| Eu | 0.644 | 0.232 | −0.052 | 1.000 | 0.515 | 0.109 | 0.704 | −0.425 | 0.685 | −0.152 | 0.592 | 0.391 | −0.190 | −0.463 | −0.785 | 0.659 |
| Gd | **0.985** | **0.953** | 0.823 | 0.515 | 1.000 | **0.904** | **0.961** | 0.474 | **0.972** | 0.558 | **0.995** | **0.990** | 0.741 | 0.508 | −0.427 | **0.915** |
| Ho | 0.830 | **0.988** | **0.986** | 0.109 | **0.904** | 1.000 | 0.779 | 0.789 | 0.798 | 0.664 | 0.864 | **0.953** | **0.943** | 0.826 | −0.058 | 0.708 |
| La | **0.993** | 0.842 | 0.670 | 0.704 | **0.961** | 0.779 | 1.000 | 0.317 | **0.998** | 0.327 | **0.982** | **0.917** | 0.540 | 0.303 | −0.491 | 0.890 |
| Lu | 0.365 | 0.686 | 0.870 | −0.425 | 0.474 | 0.789 | 0.317 | 1.000 | 0.328 | 0.403 | 0.409 | 0.575 | 0.846 | **0.967** | 0.563 | 0.126 |
| Nd | **0.997** | 0.862 | 0.691 | 0.685 | **0.972** | 0.798 | **0.998** | 0.328 | 1.000 | 0.377 | **0.990** | **0.933** | 0.572 | 0.326 | −0.504 | **0.909** |
| Sc | 0.432 | 0.689 | 0.674 | −0.152 | 0.558 | 0.664 | 0.327 | 0.403 | 0.337 | 1.000 | 0.492 | 0.628 | 0.802 | 0.613 | −0.301 | 0.617 |
| Sm | **0.997** | **0.920** | 0.770 | 0.592 | **0.995** | 0.864 | **0.982** | 0.409 | **0.990** | 0.492 | 1.000 | **0.972** | 0.674 | 0.431 | −0.471 | **0.923** |
| Tb | **0.953** | **0.985** | 0.892 | 0.391 | **0.990** | **0.953** | **0.917** | 0.575 | **0.933** | 0.628 | **0.972** | 1.000 | 0.827 | 0.619 | −0.335 | 0.878 |
| Y | 0.620 | 0.908 | **0.974** | −0.190 | 0.741 | **0.943** | 0.540 | 0.845 | 0.572 | 0.802 | 0.674 | 0.827 | 1.000 | **0.930** | 0.081 | 0.555 |
| Yb | 0.374 | 0.739 | **0.907** | −0.463 | 0.508 | 0.826 | 0.303 | 0.967 | 0.326 | 0.613 | 0.431 | 0.619 | **0.930** | 1.000 | 0.441 | 0.225 |
| *Eff. Diameter* | **0.964** | 0.849 | 0.649 | 0.669 | **0.956** | 0.761 | **0.942** | 0.207 | **0.956** | 0.562 | **0.966** | **0.919** | 0.585 | 0.277 | 1.000 | **0.990** |
| *Minor Axis* | **0.919** | 0.808 | 0.595 | 0.659 | **0.915** | 0.708 | 0.890 | 0.126 | **0.909** | 0.617 | **0.923** | 0.878 | 0.555 | 0.225 | −0.743 | 1.000 |

| | Ce | Dy | Er | Eu | Gd | Ho | La | Lu | Nd | Sc | Sm | Tb | Y | Yb | *Eff. Diameter* | *Minor Axis* |
|---|---|---|---|---|---|---|---|---|---|---|---|---|---|---|---|---|
| Study area (2): Musgrave Province | | | | | | | | | | | | | | | | |
| Ce | 1.000 | 0.891 | 0.865 | **0.931** | **0.935** | 0.88 | **0.973** | 0.873 | **0.984** | 0.115 | **0.96** | **0.915** | 0.831 | 0.856 | 0.615 | 0.0106 |
| Dy | 0.891 | 1.000 | **0.997** | **0.971** | **0.992** | **0.999** | 0.832 | **0.996** | **0.941** | 0.453 | **0.976** | **0.998** | **0.986** | **0.993** | 0.445 | −0.139 |
| Er | 0.865 | **0.997** | 1.000 | **0.955** | **0.982** | **0.999** | 0.804 | **0.997** | **0.919** | 0.473 | **0.96** | **0.991** | **0.993** | **0.997** | 0.423 | −0.177 |
| Eu | **0.931** | **0.971** | **0.955** | 1.000 | **0.981** | **0.962** | 0.848 | **0.961** | **0.98** | 0.407 | **0.992** | **0.981** | **0.921** | **0.958** | 0.563 | −0.106 |
| Gd | **0.935** | **0.992** | **0.982** | **0.981** | 1.000 | **0.988** | 0.886 | **0.982** | **0.97** | 0.375 | **0.993** | **0.997** | **0.967** | **0.976** | 0.474 | −0.073 |
| Ho | 0.88 | **0.999** | **0.999** | **0.962** | **0.988** | 1.000 | 0.823 | **0.996** | **0.93** | 0.458 | **0.969** | **0.995** | **0.991** | **0.995** | 0.429 | −0.151 |
| La | **0.973** | 0.832 | 0.804 | 0.848 | 0.886 | 0.823 | 1.000 | 0.81 | **0.926** | 0.02 | **0.902** | 0.859 | 0.786 | 0.787 | 0.531 | 0.261 |
| Lu | 0.873 | **0.996** | **0.997** | **0.961** | **0.982** | **0.996** | 0.81 | 1.000 | **0.927** | 0.501 | **0.964** | **0.991** | **0.985** | **0.998** | 0.48 | −0.135 |
| Nd | **0.984** | **0.941** | **0.919** | **0.98** | **0.97** | **0.93** | **0.926** | **0.927** | 1.000 | 0.253 | **0.99** | **0.959** | 0.882 | **0.918** | 0.615 | −0.001 |
| Sc | 0.115 | 0.453 | 0.473 | 0.407 | 0.375 | 0.458 | 0.02 | 0.515 | 0.253 | 1.000 | 0.334 | 0.425 | 0.459 | 0.506 | 0.275 | −0.079 |
| Sm | **0.96** | **0.976** | **0.96** | **0.992** | **0.993** | **0.969** | **0.902** | **0.964** | **0.99** | 0.334 | 1.000 | **0.987** | **0.934** | **0.957** | 0.542 | −0.054 |
| Tb | **0.915** | **0.998** | **0.991** | **0.981** | **0.997** | **0.995** | 0.859 | **0.991** | **0.959** | 0.425 | **0.987** | 1.000 | **0.976** | **0.987** | 0.475 | −0.102 |
| Y | 0.831 | **0.986** | **0.993** | **0.925** | **0.967** | **0.991** | 0.786 | **0.985** | 0.882 | 0.459 | **0.934** | **0.976** | 1.000 | **0.986** | 0.335 | −0.193 |
| Yb | 0.858 | **0.993** | **0.997** | **0.958** | **0.976** | **0.995** | 0.788 | **0.998** | **0.918** | 0.506 | **0.957** | **0.987** | **0.986** | 1.000 | 0.468 | −0.187 |
| *Eff. Diameter* | 0.615 | 0.445 | 0.423 | 0.563 | 0.474 | 0.429 | 0.531 | 0.48 | 0.615 | 0.275 | 0.542 | 0.475 | 0.335 | 0.468 | 1.000 | 0.286 |
| *Minor Axis* | 0.106 | −0.139 | −0.177 | −0.106 | −0.07 | −0.151 | 0.261 | −0.135 | −0.001 | −0.079 | −0.05 | −0.102 | −0.139 | −0.187 | 0.286 | 1.000 |

element distributions and rare-earth elements (REE) concentrations) and the most consistent statistically significant shape descriptors (Table 2). The list of available whole rock geochemistry data is presented in Appendix A2. Notably, all available whole rock geochemistry data for both study areas are related to granites with one exception, a dacite from the Musgrave Province (sample 187199). Mean values of significant shapes were used to identify statistically significant relationships to major elements and REEs. The correlation analysis between whole rock chemistry and grain shape is visually displayed as a correlation matrix (Appendix A3). In addition, we determined how well the data relate to each other by the calculation of the Pearson's Correlation Coefficient, denoted as 'R' (Table 5). A perfect relationship is expressed by values of either 1 or −1, which implies that a linear equation describes the relationship between any major element or REE and the most consistent significant shape descriptors. A value of 0 implies that there is no linear correlation between variables. The magnitude of R-values represents the strength of correlation, where values $<0.5$ are considered weakly correlated, values between 0.5 and 0.8 moderate, and values $>0.8$ as highly correlated.

## 4. Results

We identified statistically significant zircon shape descriptors in relation to $^{207}Pb/^{206}Pb$ ages and chemical composition in Archean and Proterozoic source rocks and associated Proterozoic basins. Variations of zircon grain shapes in metasedimentary rocks compared to magmatic rocks are observed (Fig. 3). Based on CL images, metamorphic zircon overgrowths are very infrequent in the studied populations and do not significantly change any grain shape relationships. Pristine idiomorphic crystal habits ranging from needle like - prismatic to short stubby shapes occur in igneous rocks, whereas detrital grains have well-rounded edges and stubby to elongated crystal shapes. Zircon grain sizes range from 80–756 μm in length and 42–425 μm in width within magmatic rocks and from 61–1077 μm in length and 44–673 μm in width within metasedimentary rocks (Appendix A1).

### 4.1. Correlations of zircon grain shapes with age, U and Th content

Results obtained by linear regression identified two statistically significant shape factors, the *Minor Axis* and *Effective Diameter* (Table 2). Both shape factors show consistently strong reoccurring correlations throughout both study regions and also in magmatic source zircons and in detrital zircons for correlations against $^{207}Pb/^{206}Pb$ age or U concentration. Other shape descriptors such as *Area* or *Perimeter* could not be consistently correlated across the entire data set or rock types. The linear regression results are documented in Table 4.

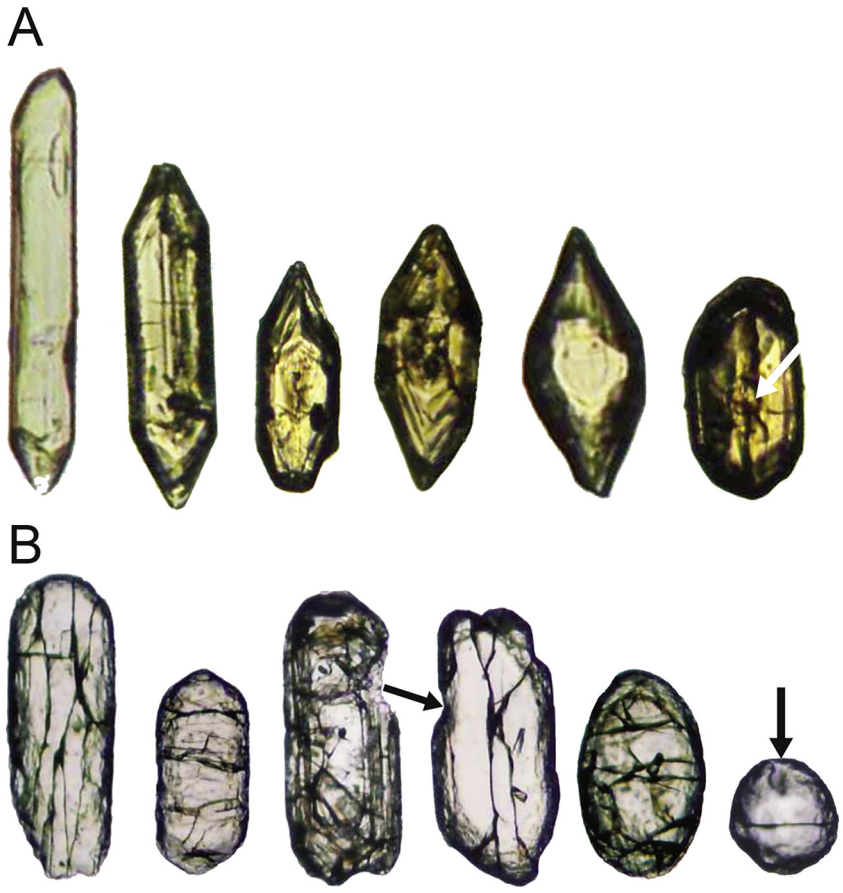


**Figure 3.** Photomicrographs of selected zircon grains (not to scale) showing the wide range of shapes and sizes from (A) Archean magmatic rocks of the Narryer Terrane/Yilgarn Craton, and (B) from Proterozoic metasedimentary rocks of the Badgeradda Group. Fracturing of detrital zircons (B) parallel c-axis or perpendicular to c-axis occurs during transport, the direction of surface pitting and edge breaking is predominantly parallel c-axis (black arrows). Roundness of zircons is determined by chemical dissolution and mechanical abrasion during transport increases (e.g. from left to right). Zircon grains from magmatic sources (A) show characteristically growth zonation during crystallization, fluid inclusions and concentric cracking (white arrow) towards the core.

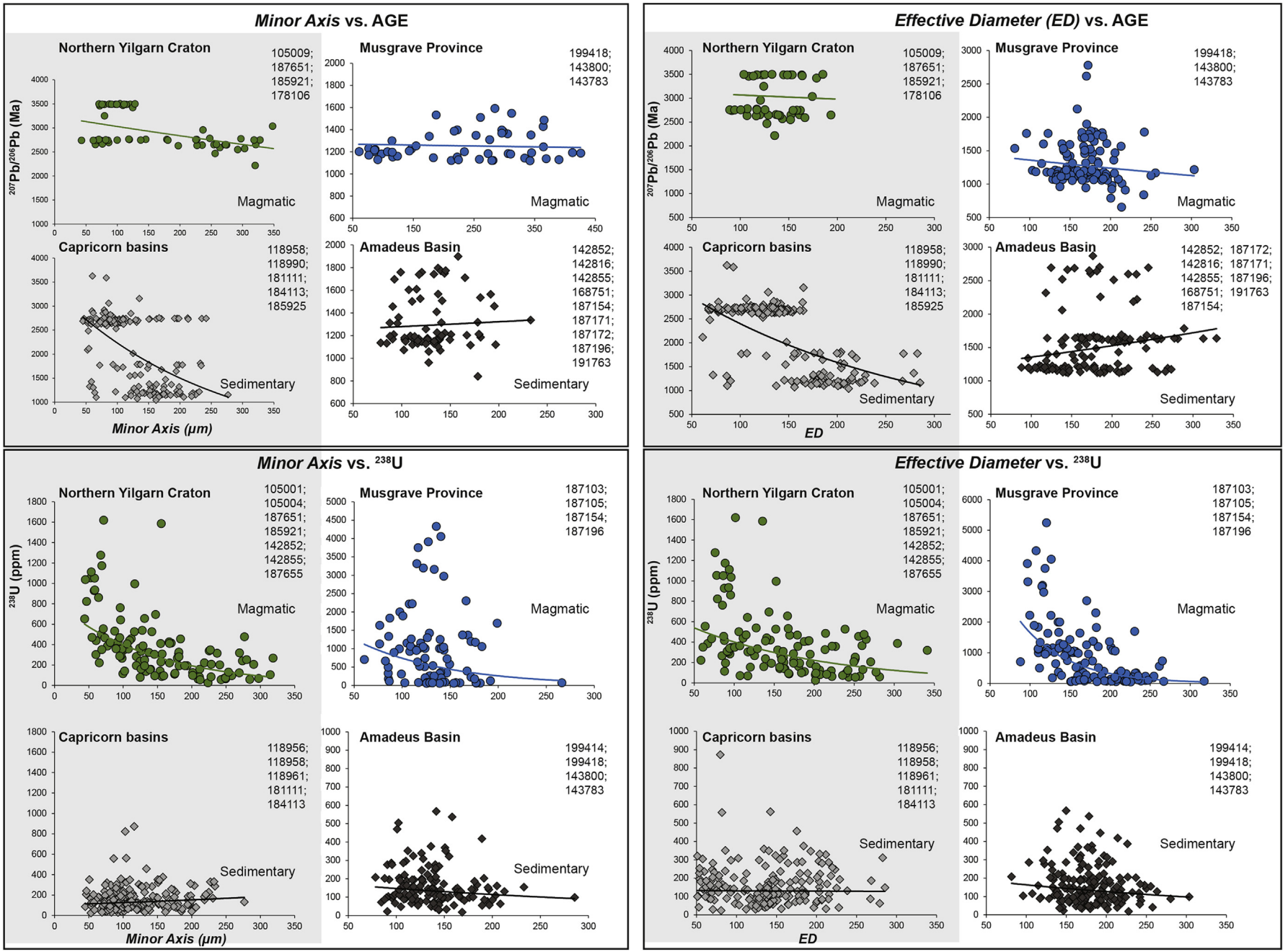


**Figure 4.** Negative linear relationships between $^{207}Pb/^{206}Pb$ ages, U content and the Minor Axis and Effective Diameter shape descriptor for both study regions in the Archean and Proterozoic. The logarithmic trend lines illustrate the rate of change in the data set within magmatic source and metasedimentary rocks. Numbers listed within each plot refer to the Geological Survey of Western Australia sample locations from which age and shape data were derived.

All analyzed zircon data show similar negative linear correlation trends between $^{207}Pb/^{206}Pb$ age, U and Th content, where the parameter with the strongest statistical significance is the absolute length of the minor axis of the grain, which is assumed to be perpendicular to c-axis (Fig. 4; Table 4). Across all samples in both study areas *Minor Axis* strongly correlates with similar distribution trends in both magmatic source rocks and detrital rocks with ages and U concentrations, whereas Th concentrations and Th/U ratios do not correlate strongly to any specific shape factor, except perhaps *Effective Diameter* in the Northern Yilgarn Craton margin and Capricorn basins region (Fig. 4). As zircon ages get younger, the length of the minor axes increases in metasedimentary and magmatic rocks. General statistics on *Minor Axis* measurements are given in Table 3, and illustrates that Archean zircon grain widths tend to be smaller compared to Proterozoic zircons. Similar trends exist for U concentrations, where decreasing U concentrations are accompanied by an increase in *Minor Axis*.

A link between different age ranges of detritus in the source relative to sink can be expressed by the erosion parameter '*K*', which expresses the relative amount of old to young sediments in a system. The *K* factor is calculated based on the equation from Allègre and Rousseau (1984) as modified after Dhuime et al. (2011):

$$K = [(\%\text{Capricorn Basins})/(\%\text{Yilgarn})]\ \textit{Sediments}/[(\%\text{Capricorn Basins})/(\%\text{Yilgarn})]\ \textit{Source} \quad (1)$$

Generally, *K* values are a function of distance and increase in value from source to sink regions. $K = 1$ is characterized by no amounts of bias introduced in sediments by erosion and $K = 4–6$ appear to represent mature drainage systems (Dhuime et al., 2011). We calculated *K* based on the published zircon ages in both source and sink areas for study region (1) and (2) using all available U–Pb geochronology from magmatic rocks and sediments. This age based *K* value is calculated from a larger data set than that derived from grain shape analysis (Appendix A4), as it represents a larger catchment area. In addition, we also calculated *K* based on the grain shape (*Minor* Axis) values from the Yilgarn–Capricorn source-sink system with Eq. (1). To calculate *K* based on the grain shape (*Minor Axis*), we calculated a width threshold of 105 μm, which is the 95% confidence level below which the grain was predicted to be Archean, and above which it was predicted to be Proterozoic. The threshold value of *Minor Axis* dimension was estimated where kernel distribution functions intersected at 129 μm (source) and 105 μm (sink) (Appendix A5). Here, we used the Gaussian kernel probability estimation that describes the distribution density of our data (here *Minor Axis* measures) based on two different ages, Archean and Proterozoic grains. The known density function is therefore averaged across the calculated data points to create a smooth approximation line. The age-based *K* value was $K = 6$ for the Yilgarn–Capricorn source-sink system and $K = 5.5$ for the Musgrave–Amadeus source-sink system. When calculated from grain width (Minor Axis) the *K* value for the Yilgarn–Capricorn source-sink region is $K = 5.3$. While not identical, the shape based value is closely comparable to the value of the age-based calculation. For the Musgrave–Amadeus system the limited age range in the source rocks did not allow meaningful kernel distribution estimations.

### 4.2. Correlation of zircon grain shapes with whole rock geochemistry

We investigated if the previously defined significant shape descriptors *Minor Axis* and *Effective Diameter* (Table 2) also showed a correlation between magmatic zircon grain shape and REE and major element concentrations of their host rock. The range of mean values in major elements and REE concentrations compared to the arithmetic mean values of the shape measures indicated a high degree of variation (Fig. 5). We analyzed the correlation relationships based on Pearson's correlation coefficient and generated pairwise scatterplots to visually asses the distribution pattern (Table 5; Appendix A3). In the Northern Yilgarn Craton and the Musgrave Province we observed high correlations between most of the REE (Ce, Dy, Gd, La, Nd, Sm, and Tb) and also between major elements, which show weaker correlations. Compared to the shape descriptor *Minor Axis* and also *Effective Diameter* no conclusive

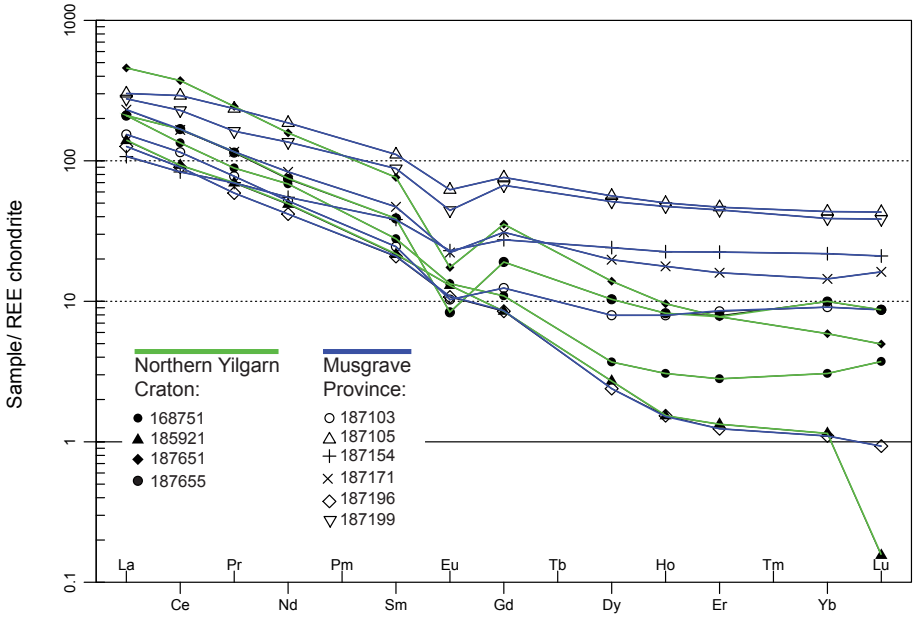


**Figure 5.** Chondrite-normalized (Boynton, 1984) REE patterns for granitoids of source regions from both case study regions.

correlation patterns were observed with whole rock chemistry (Appendix A3; Table 5).

### 4.3. Metamictization of zircon populations

The degree of metamictization was determined by using U and Th concentrations and $^{206}Pb/^{207}Pb$ ages to calculate the dose of α-events for each zircon grain (Murakami et al., 1991). We found that zircon grains in magmatic source rocks range in apparent density between 4.74 and 4.01 g/cm$^3$, and in metasedimentary rocks between 4.75 and 4.26 g/cm$^3$ (Table 6; complete data set in Appendix A6). Zircon grains were classified as 'highly crystalline' when alpha dose was $<3$ α/mg $\times$ $10^{15}$, 'moderately damaged' when 3 and 8 α/mg $\times$ $10^{15}$ and 'highly metamict' when $>8$ α/mg $\times$ $10^{15}$. Highly crystalline, high density zircons dominate the population in both metasedimentary and magmatic rocks. The population of highly metamict grains accounts for up to 12% in magmatic rocks, but is apparently completely missing from the detrital population, with only up to 6% of the metasedimentary zircon population classified as in a 'moderate' metamict state.

## 5. Discussion

Our correlation results from comparing zircon grain shapes across two different source-sink regions in Western Australia, with different age spans and tectonic settings, show that the interpretation of source-sink relationships and the assessment of preservation bias within the detrital record can be enhanced by analyzing morphological variations in zircon grains. The detrital zircon age spectra from the two study regions retain the main age components of the magmatic zircon record (Fig. 6). However, potential transport distances play an important role on the preservation of zircon grains, as relatively low numbers of metamict grains are found within the sediments compared to the magmatic population.

Our findings show a statistically significant correlation throughout the entire data set from both study areas between the most dominant shape descriptor *Minor Axis* (and to a certain degree *Effective* Diameter) and age and also with zircon U concentration, for both magmatic source and metasedimentary host rocks (Table 4). Shape descriptors that exhibit inconsistent intervals (p-values $\leq$ 0.05) were interpreted as inconclusive results and therefore not suitable for conclusive shape correlations with age and U concentration. The modification of zircon shapes during transport is most likely controlled by the integrity of the lattice structure. As the long axis (*Major Axis*) and the *Aspect Ratio* showed no statistical significance with age and grain chemistry, pitting and abrasion may preferentially have occurred on the prism faces, ultimately resulting in segmentation of the grains perpendicular to c-axis. It is likely that elongated grains (aspect ratio greater than 3:1) preferably fracture into shorter grains during early stages of erosion due to mechanical abrasion and then get fragmented or even get removed from the sedimentary system by hydraulic sorting during transportation. Mechanical failure of metamict grains that have been weakened by radiation damage from α-decay of U and Th isotopes is also a likely influence on detrital populations.

In addition, we identified other statistically significant grain shape factors that correlate with age and grain chemistry, such as *Effective Diameter*, *Roundness*, *Circularity*, and *Perimeter* for some samples (Table 4). Caution must be taken when interpreting these shape descriptors, since they are not consistently significant throughout the entire data set, and we therefore consider them inconclusive. It appears that grain shapes based on *Effective Diameter*, *Roundness*, *Circularity*, and *Perimeter* occasionally remain constant during sediment transport. An increase in grain size, calculated from *Roundness* and *Perimeter* measures, correlates with statistical significance to a decrease in age. This is consistent with the summary statistics produced from *Minor Axis* shape measures, which show that the Archean magmatic grains are overall smaller than Proterozoic grains (Table 3). The statistical inconclusiveness of the shape descriptors *Effective Diameter*, *Roundness*, *Circularity*, and *Perimeter* in zircon grains appear to be sensitive to potential transport distances and are a function of proximity to source with grain surface damage by mechanical abrasion caused by erosional processes in the sedimentary system. We do not observe any strong links between whole rock geochemistry and zircon morphologies (Table 5; Appendix A3). Our results suggest that Archean and Proterozoic zircon grains from magmatic source rocks and associated metasedimentary rocks increase in *Minor Axis* (Table 2) length with decreasing age, whereas the prism faces {100} and {110} are widely variable and have no clear correlation. The same trend is also displayed for U concentration, in which low concentrations are linked to an increase in grain width (e.g. *Minor Axis*). These observations can be explained by the structural properties of the zircon crystal ($ZrSiO_4$ consisting of ca. 2/3 $ZrO_2$ and ca. 1/3 $SiO_2$), which is composed of chains of alternating edge-sharing $SiO_4$ tetrahedra and $ZrO_8$ triangular dodecahedra aligned parallel to the c axis (e.g. Robinson et al., 1971; Kolesov et al., 2001). Structural damage of metamict zircon grains results in the loss of density and hardness as a result of alpha-recoil events (Ewing and Headley, 1983; Murakami et al., 1991). Radioactive decay from U and Th causes lattice displacements and occurrences of microfractures, which may have provided pathways for the addition or removal of U and Th (Chakoumakos et al., 1987; Ewing et al., 2003). Our analysis shows for the first time that changes in U concentrations affect grain width (*Minor Axis*) as we have demonstrated that higher U concentrations in zircon crystals coincide with smaller *Minor Axis* measurements. We therefore propose that elevated U content affects the growth of the {110} and {100} prism faces. U concentration is strongly correlated with grain width in Proterozoic zircon grains of the Musgraves region and Archean grains of the Yilgarn region (Fig. 4). These observations have some similarity to results described by Benisek and Finger (1993), who reported that low U concentrations in granitic melts produce zircons with large {100} prisms. Highly metamict zircon grains appear to be rare in the detrital population of sediments in both study areas, likely due to loss of highly damaged, brittle crystals that fracture easily and do not survive long enough in the sedimentary transport system to arrive in the sink region (Balan et al., 2001; Fedo et al., 2003; Hay and Dempster, 2009). Thus, this selective enrichment means dense,

**Table 6**
Apparent density calculations and metamictization stages of zircons.

| | | Zircon type | Apparent density (g/cm$^3$) | *n* | Metamict stage | (%) |
|---|---|---|---|---|---|---|
| Study region (1) | Northern Yilgarn Craton | Magmatic | 4.01–4.12 | 17 | Highly | 12.97 |
| | | | 4.14–4.50 | 49 | Moderate | 37.40 |
| | | | 4.51–4.74 | 65 | Crystalline | 49.61 |
| | Capricorn basins | Detrital | 4.26–4.50 | 8 | Moderate | 6.15 |
| | | | 4.52–4.74 | 122 | Crystalline | 93.84 |
| Study region (2) | Musgrave Province | Magmatic | 4.01–4.13 | 17 | Highly | 10.05 |
| | | | 4.15–4.49 | 67 | Moderate | 39.64 |
| | | | 4.51–4.74 | 85 | Crystalline | 50 |
| | Amadeus Basin | Detrital | 4.44 | 1 | Moderate | 1 |
| | | | 4.52–4.75 | 128 | Crystalline | 99 |

*n* = Number of analyses.

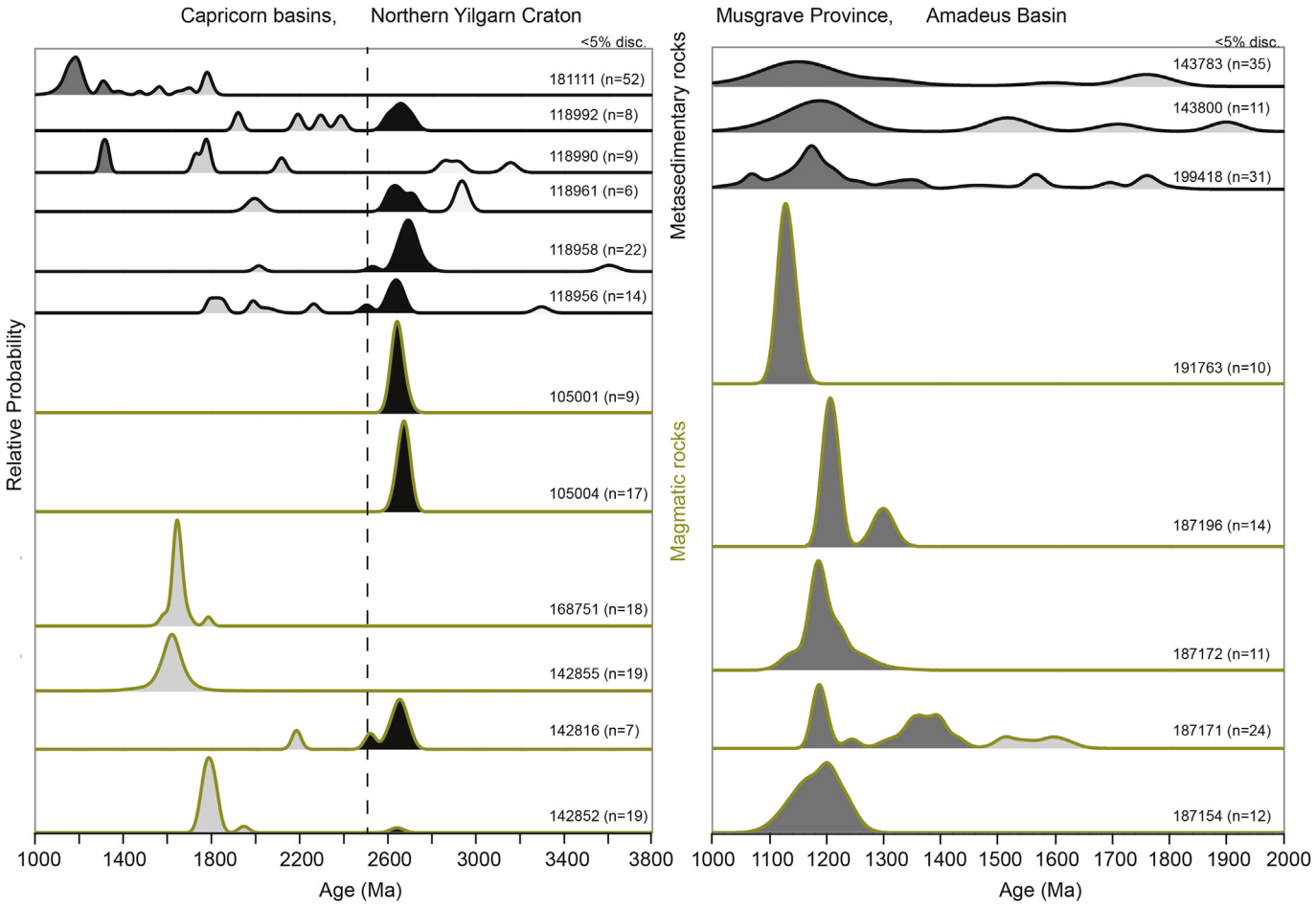


**Figure 6.** U–Pb age normalized probability plots of relevant detrital and magmatic zircon samples from both study regions (data obtained from the WACHEM data base, Geological Survey of Western Australia).

crystalline zircon grains become preferentially enriched in the sedimentary sink regions (Table 6).

Furthermore, the overall results of the linear regression indicate that although similar linear negative trends are recognized in both regions, the northern Yilgarn Craton/Capricorn basins and Musgrave Province/Amadeus Basin, and the same shape descriptors were found to be consistently significant (Fig. 4), it is not possible to accurately predict the age spectrum or U concentrations based solely on *Minor* Axis dimensions (Fig. 7; Table 3). Nonetheless, Archean grains tend to be smaller in width than Proterozoic grains and the probability that grains are more likely to be Archean is less than ~30% when the *Minor Axis* widths are above 75 μm.

The calculation of the erosion parameter *K* based on measured U–Pb ages produced a similar value in both study regions of $K = 5.5$ and $K = 6$. Such *K* values represent multicycle detrital material in a mature drainage system which sampled a considerable areas of continental crust (e.g. Dhuime et al., 2011). A similar value for *K* is calculated from the grain shape (*Minor Axis*) parameter based on the age proportions of Archean and Proterozoic material of $K = 5.3$ in study region (1). This outcome of similar *K* values based on age versus grain shape indicates that the zircon *Minor Axis* can serve as a crude proxy for source in particular geological settings where grains are sourced from disparate source regions. Also, the calculation of shape-based *K* could be used to determine the proportion of metamict detritus that was lost during transportation.

## 6. Conclusion

In this study we present the first quantitative source-sink study of zircon grain shapes based on automated digital image analysis of polished grain mounts. We have measured and statistically evaluated the shapes of 819 zircon grains relative to other variables including U and Th content, age and, where available, source rock composition from Proterozoic metasediments of the Capricorn and Amadeus basins, compared to associated source regions in their catchment areas. Based on statistical analysis of this large data set, we are able to correlate various zircon grain shape descriptors and to establish that the width of a zircon grain perpendicular to the crystallographic c-axis (the *Minor Axis* shape descriptor) best retains information from source region to sink. This means that transportation of zircon grains from magmatic source to sedimentary sink affects grain width to a much lesser extent than their length. Although highly metamict grains are preferentially lost from the detrital record, less radiation damaged zircons preserve a record from the original magmatic crystal growth processes in the form of the size of their *Minor Axis*. This study also shows that the erosional parameter (*K*), which is usually based on age, can also be calculated from detrital zircon grain shapes. While metamict zircons were preferentially removed during transport, the similarities in grain shape compared with age of source-sink zircon populations suggest that hydraulic sorting did not have a significant effect on zircon age fingerprints.

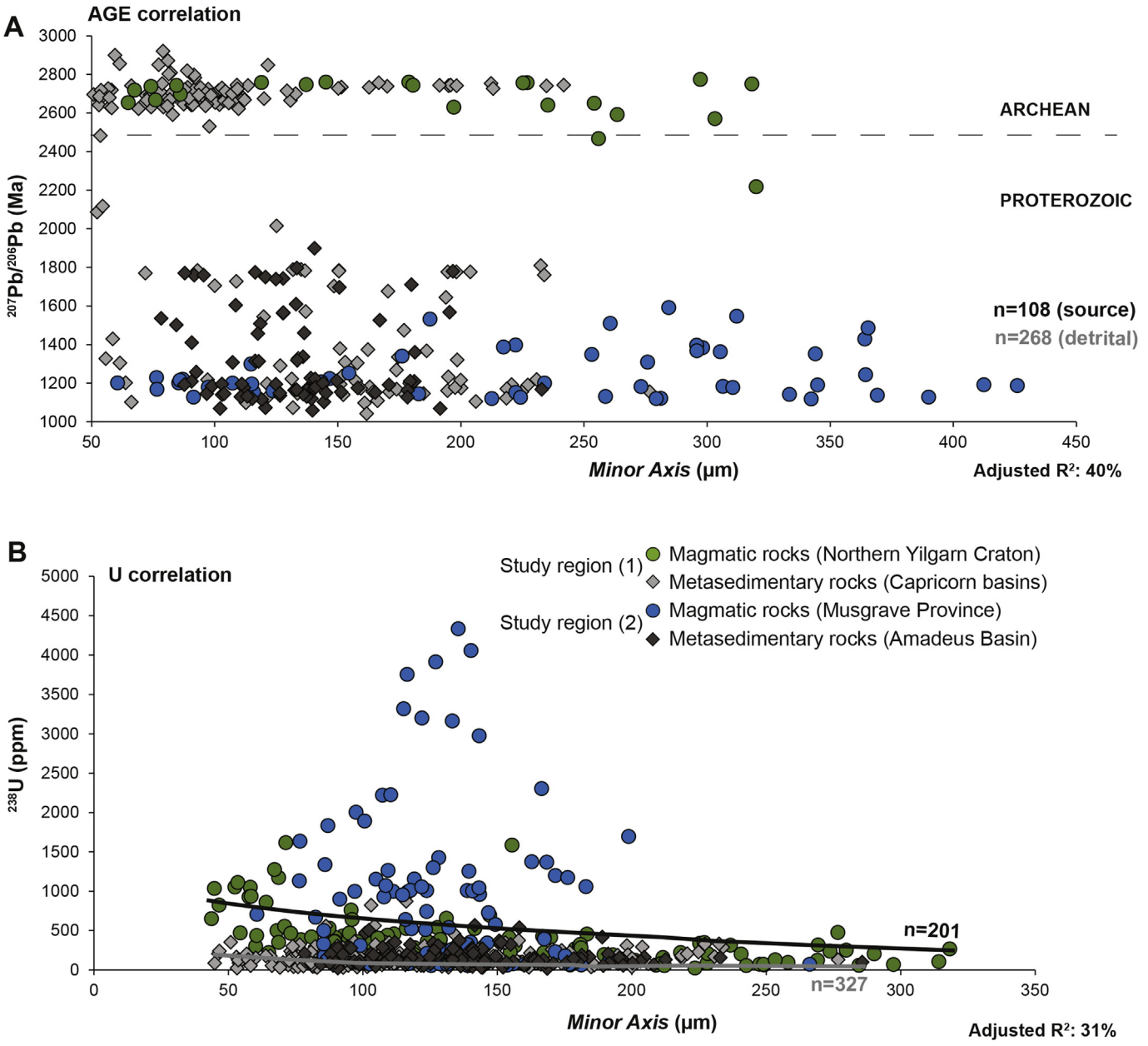


**Figure 7.** Combined distribution charts of Minor Axis measures with ages (A) and U concentrations (B) for source and sink grains for both study regions.

## Acknowledgements

We thank Marty Firth from the Centre for Applied Statistics at the School of Mathematics and Statistics (The University of Western Australia) for providing statistical advice. The Geological Survey of Western Australia is thanked for supporting this research through access to geochronology data, Klaus Gessner is thanked for helpful discussions and thorough reviews of the manuscript. We would like to thank three reviewers for their careful and constructive reviews, particularly N. Timms.

## Appendix A. Supplementary data

Supplementary data related to this article can be found at http://dx.doi.org/10.1016/j.gsf.2017.04.004.

## References

Abramoff, M.D., Magalhaes, P.J., Ram, S.J., 2004. Image processing with ImageJ. Biophotonics International 11, 36–42.
Allègre, C.J., Rousseau, D., 1984. The growth of the continent through geological time studied by Nd isotope analysis of shales. Earth and Planetary Science Letters 67, 19–34.
Andò, S., Garzanti, E., Padoan, M., Limonta, M., 2012. Corrosion of heavy minerals during weathering and diagenesis: a catalog for optical analysis. Sedimentary Geology 280, 165–178.
Balan, E., Neuville, D.R., Trocellier, P., Fritsch, E., Muller, J.-P., Calas, G., 2001. Metamictization and chemical durability of detrital zircon. American Mineralogist 86, 1025–1033.
Barclay, D.R., Buckingham, M.J., 2009. On the shapes of natural sand grains. Journal of Geophysical Research 114, B02209.
Belousova, E.A., Griffin, W.L., O'Reilly, S.Y., 2006. Zircon crystal morphology, trace element signatures and Hf isotope composition as a tool for petrogenetic modelling: examples from eastern Australian granitoids. Journal of Petrology 47, 329–353.

Benisek, A., Finger, F., 1993. Factors controlling the development of prism faces in granite zircons: a microprobe study. Contributions to Mineralogy and Petrology 114, 441–451.
Boehnke, P., Watson, E.B., Trail, D., Harrison, T.M., Schmitt, A.K., 2013. Zircon saturation re-revisited. Chemical Geology 351, 324–334.
Boynton, W.V., 1984. Cosmochemistry of the rare earth elements: meteorite studies. In: Henderson, P. (Ed.), Rare Earth Element Geochemistry. Elsevier Science, pp. 63–114.
Buick, I.S., Miller, J.A., Williams, I.S., 2001. Ordovician high-grade metamorphism of a newly recognised late Neoproterozoic terrane in the northern Harts Range, central Australia. Journal of Metamorphic Geology 19, 373–394.
Buscombe, D., 2013. Transferable wavelet method for grain-size distribution from images of sediment surfaces and thin sections, and other natural granular patterns. Sedimentology 60, 1709–1732.
Camacho, A., Armstrong, R., Davis, D.W., Bekker, A., 2015. Early history of the Amadeus Basin: implications for the existence and geometry of the Centralian Superbasin. Precambrian Research 259, 232–242.
Carroll, D., 1953. Weatherability of zircon. Journal of Sedimentary Petrology 23, 106–116.
Chakoumakos, B.C., Murakami, T., Lumpkin, G.R., Ewing, R.C., 1987. Alpha-decay induced fracturing in zircon: the transition from the crystalline to the metamict state. Science 236, 1556–1559.
Collins, W.J., Shaw, R.D., 1995. Geochronological constraints on orogenic events in the Arunta Inlier: a review. Precambrian Research 71, 315–346.
Corfu, F., Ayres, L.D., 1984. U-Pb age and genetic significance of heterogeneous zircon populations in rocks from the Favourable Lake Northwestern Ontario. Contributions to Mineralogy and Petrology 88, 86–101.
Corfu, F., Hanchar, J.M., Hoskin, P.W.O., Kinny, P., 2003. Atlas of zircon textures. Reviews in Mineralogy and Geochemistry 53, 469–500.
Cox, M.R., Budhu, M., 2008. A practical approach to grain shape quantification. Engineering Geology 96, 1–16.
DeCelles, P.G., Carrapa, B., Gehrels, G.E., 2007. Detrital zircon U-Pb ages provide provenance and chronostratigraphic information from Eocene synorogenic deposits in northwestern Argentina. Geology 35, 323–326.
Dhuime, B., Hawkesworth, C.J., Storey, C.D., Cawood, P.A., 2011. From sediments to their source rocks: Hf and Nd isotopes in recent river sediments. Geology 39, 407–410.
Ehrlich, R., Weinberg, B., 1970. An exact method for characterization of grain shape. Journal of Sedimentary Petrology 40, 205–212.
Ewing, R.C., Headley, T.J., 1983. Alpha-recoil damage in natural zirconolite ($CaZrTi_2O_7$). Journal of Nuclear Materials 119, 102–109.
Ewing, R.C., Meldrum, A., Wang, L.M., Weber, W.J., Corrales, L.R., 2003. Radiation damage in zircon. In: Hanchar, J.M., Hoskin, P.W.O. (Eds.), Zircon. Reviews in Mineralogy and Geochemistry. Mineralogical Society of America, pp. 387–425.
Fedo, C.M., Sircombe, K.N., Rainbird, R.H., 2003. Detrital zircon analysis of the sedimentary record. Reviews in Mineralogy and Geochemistry 53, 277–303.
Garzanti, E., Andò, S., Vezzoli, G., 2008. Settling equivalence of detrital minerals and grain-size dependence of sediment composition. Earth and Planetary Science Letters 273, 138–151.
Garzanti, E., Andò, S., Vezzoli, G., 2009. Grain-size dependence of sediment composition and environmental bias in provenance studies. Earth and Planetary Science Letters 277, 422–432.
Garzanti, E., Resentini, A., Andò, S., Vezzoli, G., Pereira, A., Vermeesch, P., 2015. Physical controls on sand composition and relative durability of detrital minerals during ultra-long distance littoral and aeolian transport (Namibia and southern Angola). Sedimentology 62, 971–996.
Gehrels, G., 2012. Detrital zircon U-Pb geochronology: Current methods and new opportunities. In: Busby, C., Azor, A. (Eds.), Tectonics of Sedimentary Basins: Recent Advances. Wiley-Blackwell, pp. 45–62.
Geological Survey of Western Australia, 2016. Compilation of geochronology information, 2016. Geological Survey of Western Australia digital data package. http://dmpbookshop.eruditetechnologies.com.au/product/compilation-of-geochronology-information-2016.do. ISBN:978-1-74168-680-7.
Haines, P.W., Allen, H.J., Grey, K., 2008. The Amadeus Basin in Western Australia: a forgotten corner of the Centralian Superbasin. In: Geological Survey of Western Australia, Annual Review 2008–09. Geological Survey of Western Australia, pp. 49–57.
Haines, P.W., Allen, H.J., Grey, K., Edgoose, C., 2012. The Western Amadeus Basin: Revised Stratigraphy and Correlations. Central Australian Basins Symposium III, Alice Springs, NT, pp. 1–6.
Haines, P.W., Hand, M., Sandiford, M., 2001. Palaeozoic synorogenic sedimentation in central and northern Australia: a review of distribution and timing with implications for the evolution of intracontinental orogens. Australian Journal of Earth Sciences 48, 911–928.
Haines, P.W., Kirkland, C.L., Wingate, M.T.D., Allen, H., Belousova, E.A., Gréau, Y., 2016. Tracking sediment dispersal during orogenesis: a zircon age and Hf isotope study from the western Amadeus Basin, Australia. Gondwana Research 37, 324–347.
Hand, M., Mawby, J.O., Kinny, P.D., Foden, J., 1999. U–Pb ages from the Harts Range, central Australia: evidence for early Ordovician extension and constraints on Carboniferous metamorphism. Journal of the Geological Society 156, 715–730.
Hart, N.R., Stockli, D.F., Hayman, N.W., 2016. Provenance evolution during progressive rifting and hyperextension using bedrock and detrital zircon U–Pb geochronology, Mauléon Basin, western Pyrenees. Geosphere 12, 1166–1186.
Hawke, M.L., Meffre, S., Stein, H., Hilliard, P., Large, R., Gemmell, J.B., 2015. Geochronology of the DeGrussa volcanic-hosted massive sulphide deposit and associated mineralisation of the Yerrida, Bryah and Padbury Basins, Western Australia. Precambrian Research 267, 250–284.
Hawkesworth, C., Cawood, P., Kemp, T., Storey, C., Dhuime, B., 2009. A matter of preservation. Science 323, 49–50.
Hay, D.C., Dempster, T.J., 2009. Zircon alteration, formation and preservation in sandstones. Sedimentology 56, 2175–2191.
Howard, H.M., Smithies, R.H., Kirkland, C.L., Kelsey, D.E., Aitken, A., Wingate, M.T.D., Quentin de Gromard, R., Spaggiari, C.V., 2015. The burning heart — the Proterozoic geology and geological evolution of the west Musgrave Region, central Australia. Gondwana Research 27, 64–94.
Hyslip, J.P., Vallejo, L.E., 1997. Fractal analysis of the roughness and size distribution of granular materials. Engineering Geology 48, 231–244.
Johnson, S.P., 2013. The birth of supercontinents and the Proterozoic assembly of Western Australia. Geological Survey of Western Australia, 78 p.
Kinny, P.D., Nutman, A.P., 1996. Zirconology of the Meeberrie gneiss, Yilgarn Craton, Western Australia: an early Archaean migmatite. Precambrian Research 78, 165–178.
Kirkland, C.L., Alsop, G.I., Daly, J.S., Whitehouse, M.J., Lam, R., Clark, C., 2013. Constraints on the timing of Scandian deformation and the nature of a buried Grampian terrane under the Caledonides of northwestern Ireland. Journal of the Geological Society 170, 615–625.
Kirkland, C.L., Daly, J.S., Whitehouse, M.J., 2007. Provenance and terrane evolution of the Kalak Nappe Complex, Norwegian Caledonides: implications for Neoproterozoic paleogeography and tectonics. The Journal of Geology 115, 21–41.
Kolesov, B.A., Geiger, C.A., Armbruster, T., 2001. The dynamic properties of zircon studied by single-crystal X-ray diffraction and Raman spectroscopy. European Journal of Mineralogy 13, 939–948.
Komar, P.D., 2007. The entrainment, transport and sorting of heavy minerals by waves and currents. In: Mange, M.A., Wright, D.T. (Eds.), Heavy Minerals in Use. Developments in Sedimentology. Elsevier, Amsterdam, pp. 3–48.
Lawrence, R.L., Cox, R., Mapes, R.W., Coleman, D.S., 2011. Hydrodynamic fractionation of zircon age populations. GSA Bulletin 123, 295–305.
Lindsay, J.F., 1999. Heavitree Quartzite, a Neoproterozoic (ca. 800–760 Ma), high-energy, tidally influenced, ramp association, Amadeus Basin, central Australia. Australian Journal of Earth Sciences 46, 127–139.
Lindsay, J.F., Korsch, R.J., Wilford, J.R., 1987. Timing the breakup of a Proterozoic supercontinent: evidence from Australian intracratonic basins. Geology 15, 1061–1064.
Mazzullo, J.M., Ehrlich, R., 1983. Grain-shape variation in the St. Peter sandstone: a record of eolian and fluvial sedimentation of an early Paleozoic cratonic sheet sand. Journal of Sedimentary Research 53, 105–119.
Moecher, D.P., Samson, S.D., 2006. Differential zircon fertility of source terranes and natural bias in the detrital zircon record: implications for sedimentary provenance analysis. Earth and Planetary Science Letters 247, 252–266.
Morgan, D.J., Jerram, D.A., 2006. On estimating crystal shape for crystal size distribution analysis. Journal of Volcanology and Geothermal Research 154, 1–7.
Muhling, J.R., Fletcher, I.R., Rasmussen, B., 2012. Dating fluid flow and Mississippi Valley type base-metal mineralization in the Paleoproterozoic Earaheedy Basin, Western Australia. Precambrian Research 212–213, 75–90.
Murakami, T., Chakoumakos, B.C., Ewing, R.C., Lumpkin, G.R., Weber, W.J., 1991. Alpha-decay event damage in zircon. American Mineralogist 76, 1510–1532.
Nelson, D.R., 2001. An assessment of the determination of depositional ages for Precambrian clastic sedimentary rocks by U–Pb dating of detrital zircons. Sedimentary Geology 141–142, 37–60.
Parman, S.W., 2015. Time-lapse zirconography: imaging punctuated continental evolution. Geochemical Perspectives Letters 1, 43–52.
Perry, W.J., Dickins, J.M., 1960. The Geology of the Badgeradda Area, Western Australia, vol. 46. Department of National Development, Bureau of Mineral Resources, Geology and Geophysics, 38 p.
Pirajno, F., Hocking, R.M., Reddy, S.M., Jones, A.J., 2009. A review of the geology and geodynamic evolution of the Palaeoproterozoic Earaheedy Basin, Western Australia. Earth-Science Reviews 94, 39–77.
Pirajno, F., Jones, J.A., Hocking, R.M., Halilovic, J., 2004. Geology and tectonic evolution of Palaeoproterozoic basins of the eastern Capricorn Orogen, Western Australia. Precambrian Research 128, 315–342.
Pirajno, F., Occhipinti, S.A., 2000. Three Palaeoproterozoic basins – Yerrida, Bryah and Padbury – Capricorn Orogen, Western Australia. Australian Journal of Earth Sciences 47, 675–688.
Poldervaart, A., 1956. Zircon in rocks. 2. Igneous rocks. American Journal of Science 254, 521–554.
Pupin, J.P., 1980. Zircon and granite petrology. Contributions to Mineralogy and Petrology 73, 207–220.
Rasmussen, B., Fletcher, I.R., 2002. Indirect dating of mafic intrusions by SHRIMP U–Pb analysis of monazite in contact metamorphosed shale: an example from the Palaeoproterozoic Capricorn Orogen, Western Australia. Earth and Planetary Science Letters 197, 287–299.
Rasmussen, B., Fletcher, I.R., Bekker, A., Muhling, J.R., Gregory, C.J., Thorne, A.M., 2012. Deposition of 1.88-billion-year-old iron formations as a consequence of rapid crustal growth. Nature 484, 498–501.
Roberts, N.M.W., Spencer, C.J., 2015. The zircon archive of continent formation through time. In: Roberts, N.M.W., Van Kranendonk, M., Parman, M., Shirey, S.,

Clift, P.D. (Eds.), Continent Formation through Time, vol. 389. Geological Society London, pp. 197–225.
Robinson, K., Gibbs, G.V., Ribbe, P.H., 1971. The structure of zircon: a comparison with garnet. The American Mineralogist 56, 782–790.
Russ, J.C., 2002. The Image Processing Handbook, fourth ed. CRC Press.
Schneider, C.A., Rasband, W.S., Eliceiri, K.W., 2012. NIH Image to ImageJ: 25 years of image analysis. Nature Methods 9, 671–675.
Schuiling, R.D., de Meijer, R.J., Riezebos, H.J., Scholten, M.J., 1985. Grain size distribution of different minerals in a sediment as a function of their specific density. Geologie en Mijnbouw 64, 199–203.
Scoates, J.S., Chamberlain, K.R., 1995. Baddeleyite ($ZrO_2$) and zircon ($ZrSiO_4$) from anorthositic rocks of the Laramie anorthosite complex, Wyoming: Petrologic consequences and U-Pb ages. American Mineralogist 80, 1317–1327.
Scrimgeour, I.R., Kinny, P.D., Close, D.F., Edgoose, C.J., 2005. High-T granulites and polymetamorphism in the southern Arunta Region, central Australia: evidence for a 1.64 Ga accretional event. Precambrian Research 142, 1–27.
Serra, J., 1982. Image Analysis and Mathematical Morphology, vol. 1. Academic Press, London, 610 p.
Shaw, R.D., Etheridge, M.A., Lambeck, K., 1991. Development of the Late Proterozoic to Mid-Paleozoic, intracratonic Amadeus Basin in central Australia: a key to understanding tectonic forces in plate interiors. Tectonics 10, 688–721.
Sheppard, S., Fletcher, I.R., Rasmussen, B., Zi, J.-W., Muhling, J.R., Occhipinti, S.A., Wingate, M.T.D., Johnson, S.P., 2016. A new Paleoproterozoic tectonic history of the eastern Capricorn Orogen, Western Australia, revealed by U-Pb zircon dating of micro-tuffs. Precambrian Research 286, 1–19.
Sheppard, S., Occhipinti, S.A., Tyler, I.M., 2003. The relationship between tectonism and composition of granitoid magmas, Yarlarweelor Gneiss Complex, Western Australia. Lithos 66, 133–154.
Simigian, S., Starkey, J., 1986. Automated grain shape analysis. Journal of Structural Geology 8, 589–592.
Sircombe, K.N., 2000. Quantitative comparison of large sets of geochronological data using multivariate analysis: a provenance study example from Australia. Geochimica et Cosmochimica Acta 64, 1593–1616.
Sircombe, K.N., Stern, R.A., 2002. An investigation of artificial biasing in detrital zircon U-Pb geochronology due to magnetic separation in sample preparation. Geochimica et Cosmochimica Acta 66, 2379–2397.
Smithies, R.H., Howard, H.M., Evins, P.M., Kirkland, C.L., Kelsey, D.E., Hand, M., Wingate, M.T.D., Collins, A.S., 2011. High-temperature granite magmatism, crust–mantle interaction and the mesoproterozoic intracontinental evolution of the Musgrave Province, Central Australia. Journal of Petrology 52, 931–958.
Soille, P., Vincent, L.M., 1990. Determining watersheds in digital pictures via flooding simulations. Visual Communications and Image Processing 90, 240. Lausanne, Switzerland.
Spencer, C.J., Cawood, P.A., Hawkesworth, C., Roberts, N.M.W., 2013. The isotopic artifacts of enhanced crustal preservation in collisional orogenesis. Mineralogical Magazine 77, 2245.
Spencer, C.J., Kirkland, C.L., Taylor, R.J.M., 2016. Strategies towards statistically robust interpretations of in situ U–Pb zircon geochronology. Geoscience Frontiers 7, 581–589.
Syverud, K., Chinga, G., Johnsen, P.O., Leirset, I., Wiik, K., 2007. Analysis of lint particles from full-scale printing trials. Appita Journal: Journal of the Technical Association of the Australian and New Zealand Pulp and Paper Industry 60, 286–290.
Vavra, G., 1990. On the kinematics of zircon growth and its petrogenetic significance: a cathodoluminescence study. Contributions to Mineralogy and Petrology 106, 90–99.
Vavra, G., Schmid, R., Gebauer, D., 1999. Internal morphology, habit and U–Th–Pb microanalysis of amphibolite-to-granulite facies zircons: geochronology of the Ivrea Zone (Southern Alps). Contributions to Mineralogy and Petrology 134, 380–404.
Wade, B.P., Kelsey, D.E., Hand, M., Barovich, K.M., 2008. The Musgrave Province: stitching north, west and south Australia. Precambrian Research 166, 370–386.
Watson, E.B., Harrison, T.M., 1983. Zircon saturation revisited: temperature and composition effects in a variety of crustal magma types. Earth and Planetary Science Letters 64, 295–304.
Wilde, S.A., Valley, J.W., Peck, W.H., Graham, C.M., 2001. Evidence from detrital zircons for the existence of continental crust and oceans on the Earth 4.4 Gyr ago. Nature 409, 175–178.
Zhao, J.X., McCulloch, M.T., Bennet, V.C., 1992. Sm–Nd and U–Pb zircon isotopic constraints on the provenance of sediments from the Amadeus Basin, central Australia: evidence for REE fractionation. Geochimica et Cosmochimica Acta 56, 921–940.